Lithos 212–215 (2015) 353–367

Contents lists available at ScienceDirect

Lithos

journal homepage: www.elsevier.com/locate/lithos

Late Triassic adakitic plutons within the Archean terrane of the North China Craton: Melting of the ancient lower crust at the onset of the lithospheric destruction

Chao Wang [a], Shuguang Song [a,b,*], Yaoling Niu [b,c], Li Su [d]

[a] MOE Key Laboratory of Orogenic Belts and Crustal Evolution, School of Earth and Space Sciences, Peking University, Beijing 100871, China
[b] Department of Earth Sciences, Durham University, Durham DH1 3LE, UK
[c] Institute of Oceanology, Chinese Academy of Science, Qingdao 266071, China
[d] Institute of Earth Sciences, Chinese University of Geosciences, Beijing 100083, China

ARTICLE INFO

Article history:
Received 23 August 2014
Accepted 26 November 2014
Available online 4 December 2014

Keywords:
Adakitic plutons
Melting of the Paleoproterozoic lower crust
Crustal destruction in the Late Triassic
North China Craton (NCC)

ABSTRACT

We present the results of a geochemical and geochronological study for Late Triassic (230 220 Ma) adakitic plutons within the Archean terrane of the eastern part of the North China Craton (NCC). These plutons show adakitic signatures with high Sr, Sr/Y, $(La/Yb)_N$, and low Cr and Ni. The enriched Nd–Hf isotopic compositions ($\varepsilon_{Nd}(t) = -13.3$ to -12.9; $\varepsilon_{Hf}(t) = -17.4$ to -14.6) and old Nd ($T_{DM2} = 2078$–2037 Ma) and Hf ($T_{DM2} = 2366$–2192 Ma) isotope model ages suggest that the adakitic pluton may be derived from the underplated mafic lower crust of Paleoproterozoic age. The relatively low Cr and Ni contents and lower $\varepsilon_{Nd}(t)$ and $\varepsilon_{Hf}(t)$ values of the Taili adakitic plutons imply negligible input of mantle materials. Calculations of equilibrium mineral assemblages and modeling of trace element partition between melts and residual phases at different pressures confirm the interpretation that the petrogenesis of the Taili adakitic plutons is consistent with partial melting of the Paleoproterozoic mafic lower crust at 10–12 kbar (36–43 km) with a garnet granulite residue. Melting of the ancient mafic lower crust may be triggered by excess heating of the upwelling mantle in an extensional setting evoked by the contemporary subduction toward beneath the NCC from both north and south, which could serve as one possible mechanism for the destruction or lithospheric thinning of the NCC. Complex mantle–crust interaction through various mechanisms may have been responsible for the long-lived process of destruction or lithospheric thinning, which might have begun as early as in the late Triassic.

1 . Introduction

The destruction or lithospheric thinning of a stable Archean craton like the North China Craton (NCC) has been a subject of both extensive and intensive research for many years (e.g., Gao et al., 2004; Menzies et al., 1993; Niu, 2005, 2014; Xu, 2001; Yang et al., 2008, 2010). However, the timing for the destruction or lithospheric thinning of the NCC remains controversial, such as Late Carboniferous–Late Triassic (Xu et al., 2009), Late Triassic (Yang and Wu, 2009; Yang et al., 2007), Late Jurassic (Gao et al., 2004), Early Cretaceous (Wu et al., 2005b) or Late Cretaceous–Cenozoic (Li et al., 2012; Zhu et al., 2012). Various mechanisms have been proposed to explain the lithosphere thinning, including coupled thermo-mechanical and chemical erosion at the lithosphere–asthenosphere interface with the thick (>180 km), cold and refractory lithospheric keel replaced by a thin (<100 km), hot and fertile lithosphere (Menzies et al., 1993; Xu, 2001), delamination/foundering of thickened mafic lower continental crust together with the mantle lithosphere into the asthenosphere (Gao et al., 2004), peridotite–melt interaction to remove the Archean lithospheric keel (Zhang et al., 2007), crustal detachment leading to thinning of both the crust and the lithosphere (Liu et al., 2008), basal hydration weakening that physically transforms the lithospheric keel into properties of asthenosphere (Niu, 2005), lithospheric folding-induced removal of lithospheric mantle (Zhang, 2012), and the formation of the seismic low velocity zone (LVZ) beneath the entire eastern China (not restricted to the NCC) in response to dehydration of the paleo-Pacific slab that lies in the mantle transition zone beneath eastern China (Niu, 2014).

Adakitic rocks, originally defined as intermediate to felsic igneous rocks with geochemical signatures of high Sr, low Y and highly fractionated REE patterns (Defant and Drummond, 1990), commonly occur in some modern arc settings and are thought to form by partial melting of the subducting/subducted young and hot oceanic crust (Defant and Drummond, 1990; Martin et al., 2005), or through a variety of other mechanisms (see Castillo, 2012). Adakitic rocks have also been found in orogenic belts on land, interpreted as resulting from melting of the newly underplated or thickened mafic lower crust (e.g., Atherton and

* Corresponding author at: MOE Key Laboratory of Orogenic Belts and Crustal Evolution, School of Earth and Space Sciences, Peking University, Beijing 100871, China.
E-mail address: sgsong@pku.edu.cn (S. Song).

http://dx.doi.org/10.1016/j.lithos.2014.11.027

Petford, 1993; Chung et al., 2003) or decompression melting of subducted ocean crust in response to continental collision and exhumation (Song et al., 2014).

In the past decades, many Mesozoic granitoids with adakitic signature have been reported in the NCC, which are obviously unrelated to active subduction, but formed in an intracontinental setting (Gao et al., 2004; Jiang et al., 2007; Ma et al., 2012; Xu et al., 2002). They share the same geochemical characteristics of most adakites and adakitic rocks but have high K_2O contents (Rapp et al., 2002). The mafic lower continental crust was thought to play an important role in their petrogenesis through speculated processes such as delamination or foundering (Gao et al., 2004; Xu et al., 2002) although it remains unknown how and why the buoyant mantle lithosphere can delaminate with the overlaying crust melting in the asthenospheric conditions. Thus, these adakitic rocks are interpreted as indicating the NCC lithospheric thinning in the Mesozoic (Wu et al., 2005a; Yang and Wu, 2009).

In this paper, we present results of detailed geochemical and geochronological study of Late Triassic adakitic plutons within the Archean terrane of the NCC at the coast of the Bohai Sea, Western Liaoning, China. The aims of this paper are 1) to evaluate the petrogenesis of these plutonic rocks, 2) to place constraints on the lithological

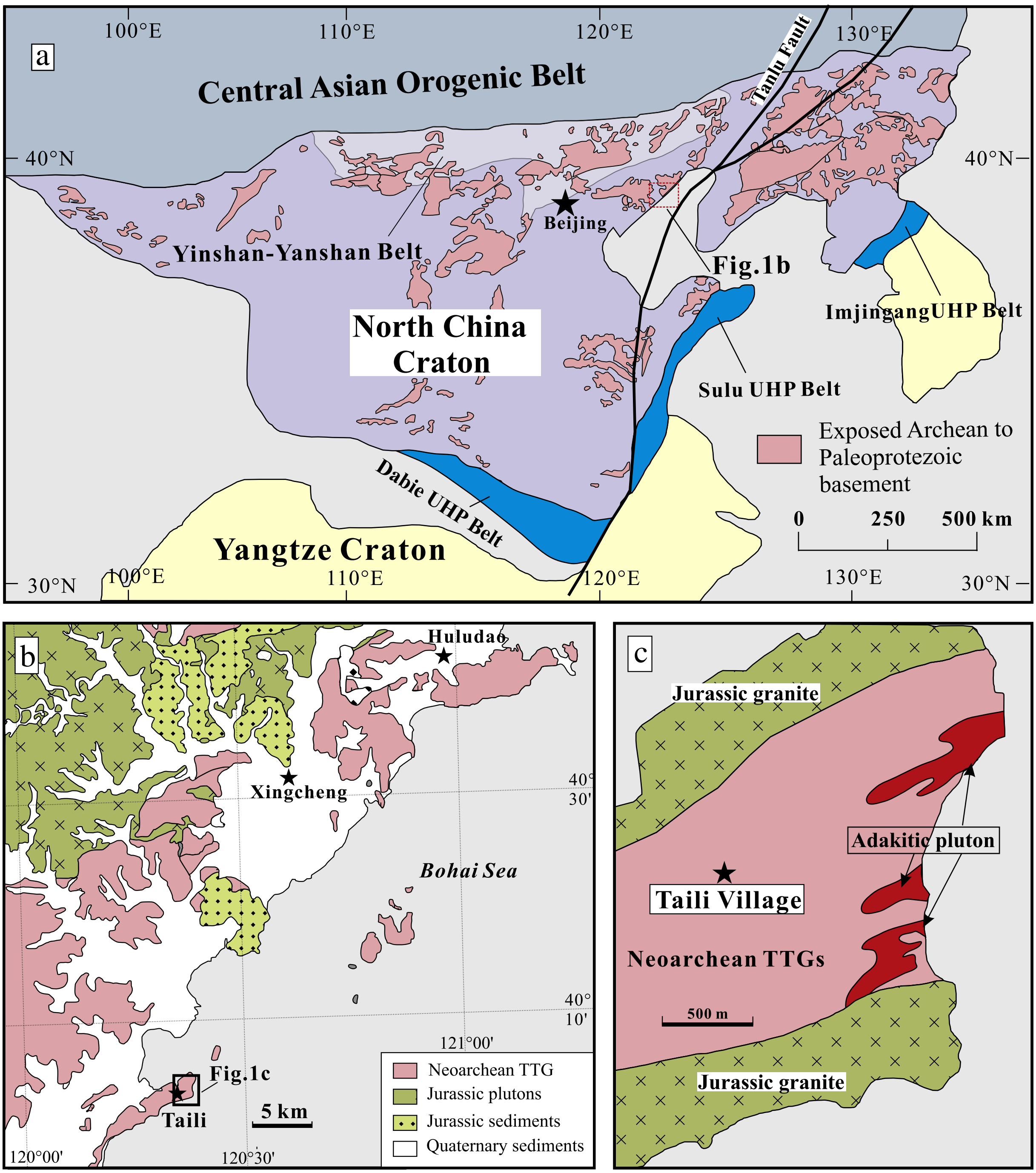

Fig. 1. (a) Schematic map showing major tectonic units of continental China and Korean peninsula (modified after Zhao et al., 2005). (b) Simplified geological map of the Xingcheng area. (c) Geological map of the Taili Beach.

properties of the lower crust and 3) to limit the onset timing of the lithospheric thinning beneath the NCC.

2 . Geological background and samples

The NCC is the largest and oldest craton in China and preserves remnants of ≥3.8 Ga crust (Liu et al., 1992). It was generally thought to be formed by collision of two distinct Archean blocks, i.e., the Eastern block and the Western block, along the Trans-North China Craton Orogen in the Late Paleoproterozoic (~1.85 Ga) (e.g., Zhao et al., 2005) (Fig. 1a). From the Late Paleoproterozoic (~1.85 Ga) to the end of Paleozoic (~250 Ma), there were no significant tectonothermal events except for some anorogenic (mantle plume-related) magmatic events in 2.3–2.1 Ga, ~1.78 Ga, 1.35–1.31 Ga and 0.9 Ga in the Archean nuclei (Peng et al., 2008, 2011, 2012; Zhang et al., 2009a, 2012a). The Paleozoic diamondiferous kimberlites in the eastern Block of the NCC suggest that the NCC must have had a thick cratonic lithosphere in the Paleozoic (Menzies et al., 1993; Zhang et al., 2010). However, since the Mesozoic, the eastern part of the NCC has undergone extensive tectonothermal events and resulted in intense deformation, magmatism and mineralization (Yang and Wu, 2009; Yang et al., 2003).

The NCC is bounded by the Triassic Qinling–Dabie–Sulu orogenic belt to the south and east (Li et al., 1993) and the Late Paleozoic Central Asian Orogenic Belt (CAOB) to the north (Windley et al., 2007). It is also cut by the Tan-Lu strike-slip fault in the east. The Qinling–Dabie–Sulu orogenic belt resulted from continental collision of the NCC with the Yangtze Craton in the Triassic. The northward subduction of the seafloor leading edge of the Yangtze Craton has been interpreted as the driving force to weaken the integrity of the NCC lithosphere (Li et al., 1993; Zhang et al., 2002). The CAOB was formed by the southward subduction of the Paleo-Asian oceanic slab and arc–arc collision followed by arc–continent collision during the Late Paleozoic (Windley et al., 2007). The southward subduction and the following collision might have been responsible for the Yinshan–Yanshan intraplate fold and thrust belt on the northern margin of the NCC (Davis et al., 2001).

In the eastern part of the NCC, Mesozoic igneous rocks are widespread. Detailed geochronological studies suggest that these igneous rocks can be divided into three groups: Triassic (230–210 Ma), Jurassic (180–153 Ma) and Early Cretaceous (135–110 Ma) (Wu et al., 2005a, 2005b; Yang and Wu, 2009). Compared with the Early Cretaceous giant igneous event, the Triassic igneous rocks are sporadically distributed, including intermediate-felsic rocks, alkaline intrusives and mafic–ultramafic complexes in the northern NCC (Yan et al., 1999; Zhang et al., 2012b, 2014).

The study area is located in the central-eastern NCC, west of the Tan-Lu fault, where Jurassic granitoids are widespread on the Paleoproterozoic to Neoarchean basement (Fig. 1b). The samples of this study were collected from Taili Beach, Xingcheng City, Western Liaoning (Fig. 1c). They occur as several small plutons, showing strong foliation apparently as porphyritic granitic gneiss or mylonite deformed together with the wall rock of the Neoarchean TTGs (Fig. 2a). These plutons are dark gray with scattered, clockwise rotated plagioclase phenocrysts (Fig. 2b). They consist of K-feldspar (10–15%), plagioclase (45–50%), quartz (20–25%) and hornblende (10–15%), with minor biotite (<5%) and accessory sphene, apatite and zircon.

3 . Analytical methods

3.1 . Bulk rock major and trace element analyses

Bulk rock major and trace element analysis was done in the Geological Lab Center, China University of Geosciences, Beijing (CUGB). Major elements were analyzed using a Leeman Prodigy inductively coupled plasma-optical emission spectroscopy (ICP-OES) system with high dispersion Echelle optics. Based on rock standards AGV-2, W-2 (US Geological Survey: USGS), GRS-1 and GSR-3 (national geological standard reference material of China), the analytical precisions (1σ) for most major elements are better than 1% with the exception of TiO_2 (~1.5%) and P_2O_5 (~2.0%) (Appendix Tables 3 and 5). Loss on ignition (LOI) was determined by placing 1 g of samples in the furnace at 1000 °C for several hours before being cooled in a desiccator and reweighed.

Bulk rock trace element analysis was done on an Agilent-7500a inductively coupled plasma mass spectrometry (ICP-MS) in the Institute of Earth Science, China University of Geosciences, Beijing. About 40 mg of sample powder was dissolved in equal mixture of subboiling distilled HNO3 and HF with a Teflon digesting vessel on a hot-plate at 185 °C for 48 h using high-pressure bombs for digestion/dissolution. The sample was then evaporated to incipient dryness, refluxed with 6 N HNO_3,&& and heated again to incipient dryness. The sample was again dissolved in 2 mL of 3 N HNO_3 in high-pressure bombs for a further 24 h to ensure complete digestion/dissolution. The sample is finally diluted with Milli-Q water (18 MΩ) to a final dilution factor of 2000 in 2% HNO_3 solution. Rock standards AGV-2, W-2 and BHVO-2 (USGS) were used to monitor the analytical accuracy and precision (Appendix Tables 4 and 5). Analytical accuracy, as indicated by relative difference between measured and recommended values is better than 5% for most elements, and 10 ~ 15% for Cu, Zn, Gd and Ta.

3.2 . In-situ zircon U–Pb dating

Three samples (10XC05, 10TL06 and 10TL07) were chosen for in-situ zircon U–Pb dating. Zircon grains were separated by standard

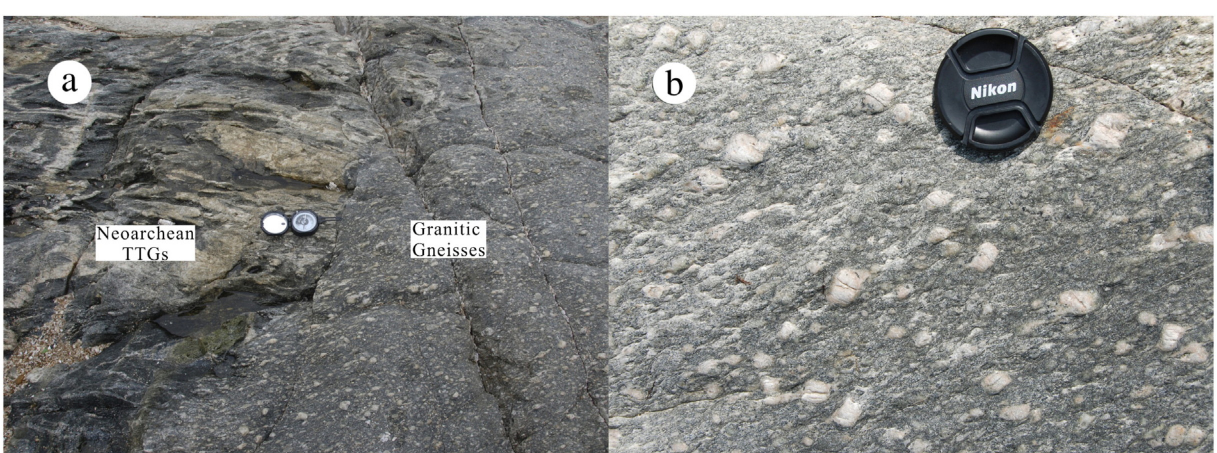

Fig. 2. (a) Field photo showing that the Taili adakitic plutons (granitic gneisses) intrude in the Neoarchean TTGs. (b) Porphyritic texture of the Taili adakitic pluton with shear foliations.

heavy-liquid and magnetic techniques, and purified by hand-picking under a binocular. They were embedded in epoxy resin discs and polished down to approximately half-sections to expose the grain centers. Cathodoluminescence (CL) images were acquired using a cathodoluminescent (CL) spectrometer (Garton Mono CL3+) equipped on a Quanta 200 F ESEM at scanning conditions of 15 kV and 120 nA at Peking University.

Measurements of U, Th and Pb in zircons were carried out on an Agilent-7500a quadrupole inductively coupled plasma mass spectrometry coupled with a New Wave SS UP193 laser sampler (LA-ICP-MS) at CUGB. Laser spot size of 36 μm, laser energy density of 8.5 J/cm^2 and a repetition rate of 10 Hz were applied for analysis. NIST 610 glass and Harvard zircon 91500 (Wiedenbeck et al., 1995) were used as external standards, Si as internal standard and zircon standard TEMORA (417 Ma) from Australia (Black et al., 2003) as secondary standard. The software GLITTER (ver. 4.4, Macquarie University) was used to process the isotopic ratios and element concentrations of zircons. The common lead correction was done following Andersen (2002). Age calculations and plots of concordia diagrams were done using Isoplot (ver. 3.0) (Ludwig, 2003). All the analytical details are described in Song et al. (2010).

3.3. In-situ zircon Hf isotope analyses

In-situ zircon Lu–Hf isotope analysis of one sample (10XC05) was carried out using a Neptune multi-collector ICP-MS attached with a New Wave UP213 laser-ablation system (LA-MC-ICP-MS) at MLR Key Laboratory of Metallogeny and Mineral Assessment, Institute of Mineral Resources, Chinese Academy of Geological Sciences, Beijing. Instrumental conditions and data acquisitions were described by Hou et al. (2007) and Wu et al. (2006). Laser spot size of 40 μm was adopted for analysis and the spots for Lu–Hf analysis were the same for U–Pb dating. Zircon GJ1 was used as the reference standard to monitor data quality during analysis, giving a weighted mean $^{176}Hf/^{177}Hf$ ratio of 0.282007 ± 7

Table 1
Major and trace element data for the Taili adakitic pluton.

Samples	10TL03	10TL04	10TL05	10TL06	10TL07	13TL02	13TL03	13TL04	13TL05	13TL06
Major elements (wt.%)										
SiO_2	70.15	69.33	69.63	68.87	69.12	69.62	68.78	68.88	68.46	68.59
TiO_2	0.33	0.35	0.4	0.38	0.38	0.33	0.31	0.35	0.32	0.31
Al_2O_3	14.67	14.34	14.84	15.05	14.96	14.96	15.37	14.96	15.24	15.33
Fe_2O_3T	2.42	2.32	2.47	2.47	2.53	2.26	2.25	2.37	2.12	2.02
MnO	0.04	0.03	0.03	0.03	0.03	0.03	0.02	0.03	0.03	0.03
MgO	1.33	1.34	1.38	1.3	1.47	1.37	1.2	1.36	1.22	1.2
CaO	1.14	2.07	2.39	1.77	2.4	2.06	1.32	2.24	1.92	2.06
Na_2O	4.4	5.06	5.5	5.26	5.24	4.57	4.98	5.07	4.4	4.38
K_2O	3.78	3.77	2.46	3.76	3.6	3.51	4.33	3.45	5.12	4.74
P_2O_5	0.15	0.23	0.29	0.25	0.12	0.19	0.2	0.2	0.19	0.18
LOI	0.93	0.42	0.6	0.85	0.36	0.65	0.77	0.64	0.55	0.72
Total	99.34	99.25	99.99	99.98	100.23	99.55	99.53	99.56	99.57	99.57
Mg#	56.1	57.4	56.6	55.0	57.5	58.6	55.4	57.2	57.3	58.1
K_2O/Na_2O	0.86	0.74	0.45	0.71	0.69	0.77	0.87	0.68	1.16	1.08
A/CNK	1.1	0.89	0.92	0.94	0.89	0.99	1.01	0.93	0.94	0.95
Trace elements (ppm)										
Rb	118.2	74.8	77.3	101.2	99.2	106.5	101.3	79.3	129.9	90.4
Ba	1689	1249	1052	1259	1170	1478	2228	1238	2344	2276
Sr	698	909	818	914	949	898	992	887	1069	1063
Cs	1.59	1.00	1.59	2.01	1.60	2.24	1.98	1.79	1.69	1.24
Th	7.24	6.63	6.98	6.89	6.78	9.24	9.21	8.8	8.09	8.49
U	1.85	2.15	2.3	2.03	2.18	2.88	2.42	2.84	2.72	2.7
Nb	15.02	13.42	15.57	15.14	13.95	15.77	13.61	16.23	15.65	18.22
Ta	0.89	0.73	1.04	0.85	0.75	0.96	0.91	1.14	1.03	1.09
Pb	16.48	18.82	19.22	18.8	16.75	24.78	28.68	25.76	26.24	26.78
Zr	144.4	134.9	148.1	155.3	158.2	148.2	153	141.8	144.7	148.6
Hf	2.75	2.61	2.83	2.97	3	3.52	3.65	3.45	3.44	3.53
Ti	2104	2072	2420	2312	2176	2134	2074	2256	2078	1989
Sc	3.62	3.47	3.73	3.58	3.5	4.31	3.96	4.27	4.12	3.83
Y	5.87	5.2	5.82	5.75	5.39	6.26	5.55	5.95	5.74	6.64
Cr	31.26	32.94	34.86	38.36	31.96	43.5	39.8	41.92	36.94	36.36
Ni	19.9	20.4	20.82	24.04	20.16	25.14	23.58	24.06	21.48	19.98
La	32.82	26.66	28.6	28.18	29.5	28.56	36.22	31.32	32.7	31.98
Ce	56.46	49.16	54.9	44.06	51.36	62.42	64.24	62.22	61.68	60.74
Pr	5.76	5.02	5.52	5.34	5.43	6.01	6.9	6.47	6.63	6.47
Nd	20	17.83	19.5	19.01	19.2	20.32	22.74	22.04	22.42	21.98
Sm	2.8	2.63	2.96	2.84	2.81	3.14	3.26	3.33	3.4	3.38
Eu	0.92	0.84	0.87	0.88	0.85	1.01	1.09	0.99	1.16	1.13
Gd	2.01	1.84	2.02	1.94	1.98	2.24	2.21	2.3	2.33	2.38
Tb	0.21	0.19	0.22	0.21	0.21	0.24	0.23	0.24	0.24	0.26
Dy	0.99	0.9	1.02	0.99	0.95	1.21	1.11	1.17	1.17	1.28
Ho	0.17	0.15	0.17	0.17	0.16	0.21	0.2	0.21	0.2	0.23
Er	0.44	0.39	0.45	0.44	0.42	0.57	0.5	0.54	0.53	0.58
Tm	0.06	0.05	0.06	0.06	0.06	0.08	0.07	0.07	0.07	0.08
Yb	0.36	0.33	0.37	0.38	0.36	0.49	0.44	0.45	0.45	0.51
Lu	0.05	0.05	0.06	0.05	0.05	0.07	0.06	0.07	0.06	0.07
TREE	123.1	106	116.7	104.5	113.3	126.6	139.3	131.4	133	131.1
Eu*/Eu	1.13	1.1	1.03	1.08	1.05	1.1	1.17	1.03	1.19	1.16
$(La/Yb)_N$	66	58	55	54	60	41	59	50	53	45
Sr/Y	119	175	141	159	176	143	179	149	186	160

N indicates chondrite-normalized.

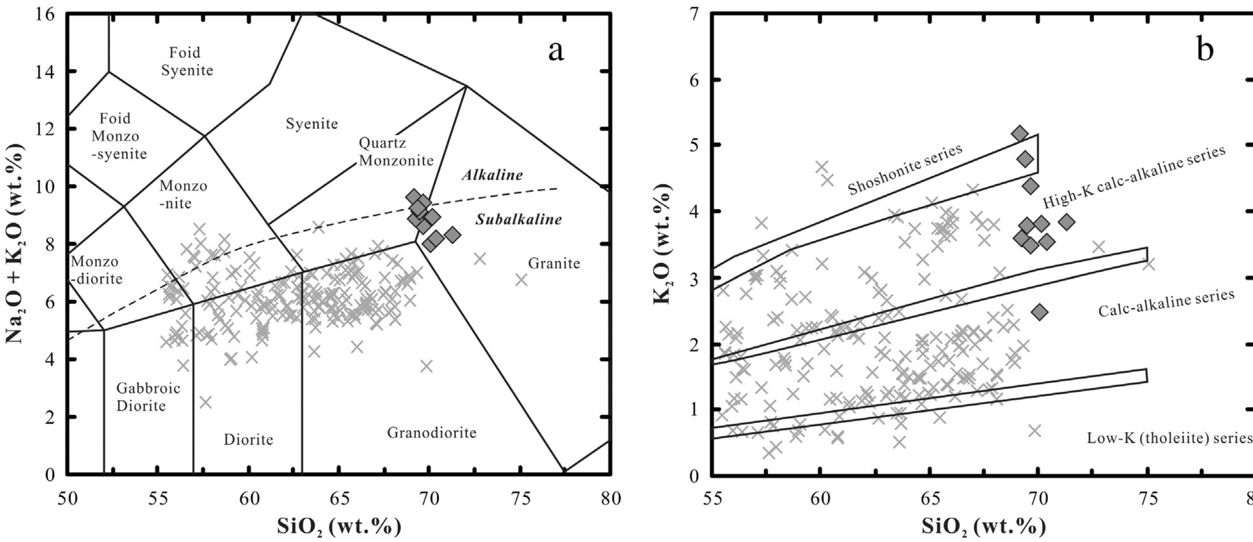

Fig. 3. (a) ($Na_2O + K_2O$)–SiO_2 diagram; (b) K_2O–SiO_2 diagram. Major oxide compositions of the Taili adakitic plutons are plotted on an anhydrous basis. Chemical compositions of typical adakites (gray crosses) are also plotted for comparison. Data sources: typical adakites including LSA and HSA, Defant et al. (1991), Samaniego et al. (2005) and references therein.

(2σ, n = 36), which is in accordance with a weighted mean $^{176}Hf/^{177}Hf$ ratio of 0.282000 ± 5 (2σ) measured by the solution analysis method (Morel et al., 2008).

3.4 . Bulk rock Sr–Nd isotope analyses

Separation and purification of Rb, Sr, Sm and Nd were done using conventional ion exchange procedures in the ultraclean lab of MOE key laboratory at Peking University. Sr and Nd isotopic ratios were measured using a Thermo-Finnigan Triton thermal ionization mass spectrometer (TIMS) at Tianjin Institute of Geology and Mineral Resources. The $^{87}Rb/^{86}Sr$ and $^{147}Sm/^{144}Nd$ ratios were calculated using ICP-MS analyses of Rb, Sr, Sm and Nd. Mass fractionation was corrected by normalizing the measured $^{87}Sr/^{86}Sr$ and $^{143}Nd/^{144}Nd$ against $^{86}Sr/^{88}Sr$ ratio of 0.1194 and $^{146}Nd/^{144}Nd$ ratio of 0.7219, respectively. Rock standard BCR-2 was used to evaluate the separation and purification process of Rb, Sr, Sm and Nd, which yielded weighted mean $^{87}Sr/^{86}Sr$ ratio of 0.704992 ± 7 (2σ, n = 94) and $^{143}Nd/^{144}Nd$ ratio of 0.512634 ± 1 (2σ, n = 97). In order to monitor the data quality during the period of data acquisition, NBS-987 Sr standard and LRIG Nd standard were analyzed and gave a weighted mean $^{87}Sr/^{86}Sr$ ratio of 0.710240 ± 2 (2σ, n = 96) and $^{143}Nd/^{144}Nd$ ratio of 0.512198 ± 3 (2σ, n = 46).

4 . Results

4.1 . Bulk rock major and trace elements

Ten fresh or least altered samples were chosen for bulk rock major and trace element analysis, and the data are reported in Table 1. All the samples are compositionally uniform with narrow ranges of SiO_2, TiO_2, Al_2O_3, MgO and $Mg^{\#}$, as well as Na_2O and K_2O/Na_2O ratios (Table 1). They plot in the quartz monzonite and granite fields on the TAS diagram (Fig. 3a), and mostly fall into the high-K calc-alkaline series field in the K_2O–SiO_2 diagram (Fig. 3b). These samples are predominantly metaluminous with A/CNK (molar $Al_2O_3/(CaO + Na_2O + K_2O)$ ratio within a narrow range of 0.89–1.01 except for sample 10TL03 (1.10; see Table 1).

All the samples have distinctly high Sr, low Y and HREEs (Fig. 4; Table 1). They show similar REE patterns with highly fractionated $(La/Yb)_N$ ratios (41–66) and a weakly positive Eu anomaly (Eu^*/Eu = 1.03–1.19) (Fig. 4a; Table 1). In the primitive mantle-normalized trace element diagram (Fig. 4b), all the samples are relatively enriched in large ion lithophile elements (LILE, e.g. Rb, Ba and Th) and depleted in high field strength elements (HFSE, i.e., Nb, Ta and Ti). Also shown is the enrichment of Sr relative to Y, thus high Sr/Y ratios (119–186). They have relatively low compatible element contents (e.g., Cr and Ni; Table 1).

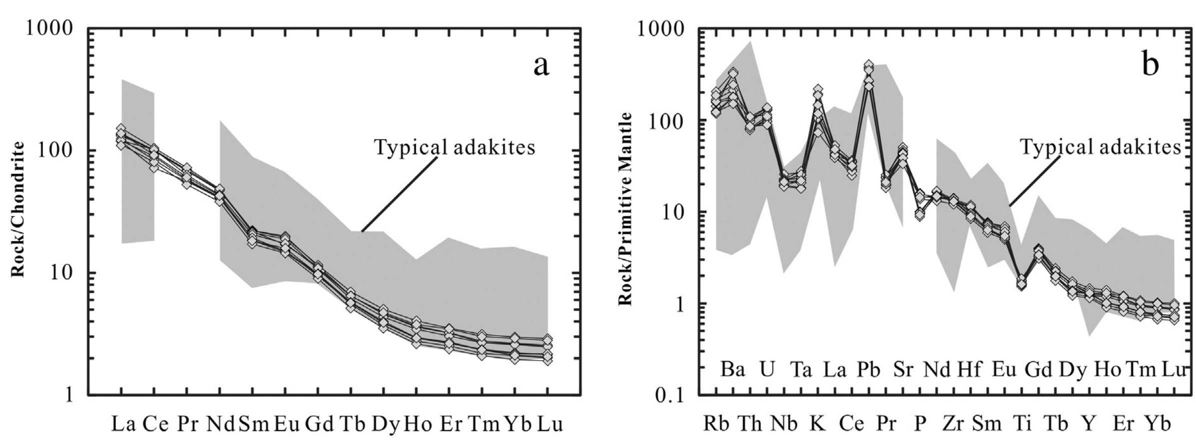

Fig. 4. (a) Chondrite-normalized REE patterns and (b) primitive mantle-normalized (PM) trace element diagram for the Taili adakitic plutons. The values of chondrite and PM are from Sun and McDonough (1989). Also plotted for comparison are those of the typical adakites. The data sources are the same as in Fig. 3.

4.2 . In-situ zircon U–Pb geochronology

Three representative samples were chosen for zircon U–Pb analysis and the data are given in Appendix Table 1 and plotted in Fig. 5. Zircon grains from these samples are euhedral and prismatic, showing oscillatory zoning of magmatic origin without any relict core in CL images (Fig. 5). The U content in zircons varies significantly from 341 to 1333 ppm, and Th from 103 to 985 ppm, with Th/U ratios of 0.23–0.89.

Twenty-five analyses for zircons from sample 10XC05 form a weighted mean $^{206}Pb/^{238}U$ age of 229.4 ± 1.2 Ma (MSWD = 0.56), twenty-five analyses for sample 10TL06 give a weighted mean $^{206}Pb/^{238}U$ age of

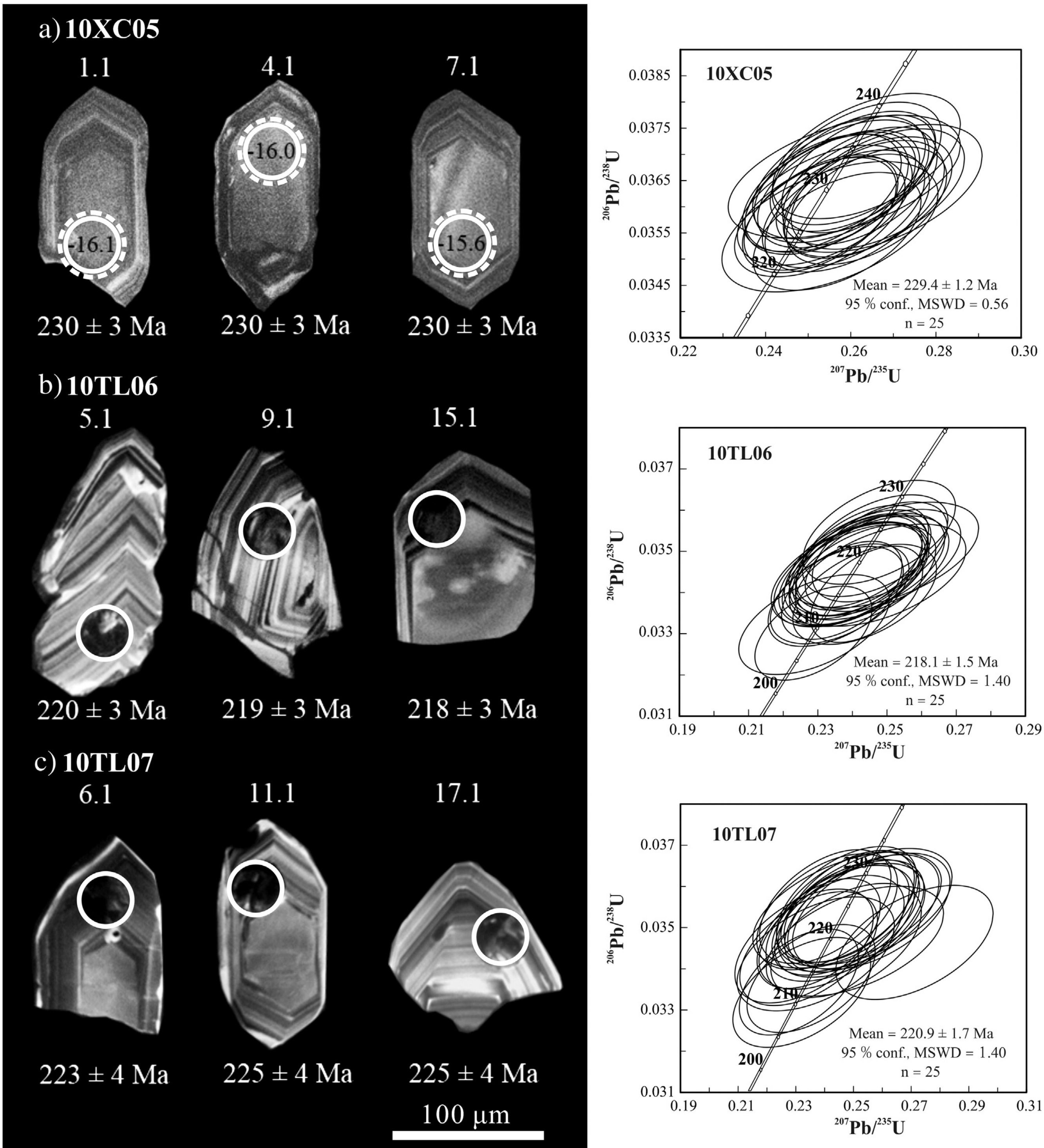

Fig. 5. Cathodoluminescence (CL) images of representative zircons and U–Pb concordia diagrams for the Taili adakitic plutons. The solid and dashed circles on the CL images are the spots of in-situ zircon U–Pb dating and Hf isotope analyses, respectively. The mean is weighted $^{206}Pb/^{238}U$ age with 95% confidence.

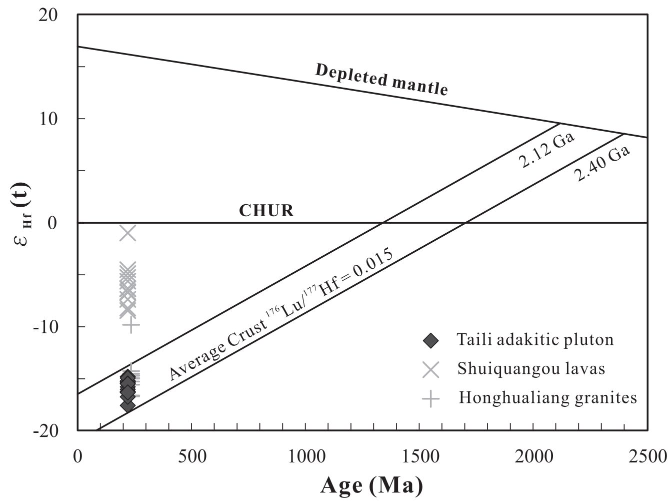

Fig. 6. $\varepsilon_{Hf}(t)$–t diagram for the Taili adakitic plutons. Also plotted for comparison are those of the Late Triassic Zhangjiakou Honghualiang granites (Jiang et al., 2007) and Shuiquangou adakitic lavas (Ma et al., 2012) on the northern margin of the NCC.

218.1 ± 1.5 Ma (MSWD = 1.40), and twenty-five analyses for sample 10TL07, 220.9 ± 1.7 Ma (MSWD = 1.40) (Fig. 5). Thus, the Taili granitoid plutons were emplaced in the Late Triassic (230–220 Ma).

4.3 . In-situ zircon Hf isotopic compositions

In-situ zircon Hf isotopic data for sample 10XC05 are given in Appendix Table 2 and plotted in Fig. 6. The crystallization age (229 Ma) was used to calculate the $\varepsilon_{Hf}(t)$ values and the two-stage depleted mantle Hf model ages (T_{DM2} ages). The data show very similar present-day $^{176}Hf/^{177}Hf$ ratios of 0.282142–0.282220 with a narrow range $\varepsilon_{Hf}(t)$ of −17.4 to −14.6, giving the two-stage depleted mantle Hf model ages (T_{DM2} ages) of 2366–2192 Ma.

4.4 . Bulk rock Sr–Nd isotopic compositions

Sr–Nd isotopic data of five representative samples are given in Table 2 and plotted in Fig. 7. The initial $^{87}Sr/^{86}Sr$ ratios ($I_{Sr}(t)$ values) and $\varepsilon_{Nd}(t)$ values were calculated using the zircon U–Pb age of 220 Ma. The samples display a narrow range of initial $I_{Sr}(t)$ = 0.704640–0.705612. The $\varepsilon_{Nd}(t)$ values are highly negative (−13.3 to −12.9), giving two-stage depleted mantle Nd model ages (T_{DM2} ages) of 2078–2037 Ma, which is similar to zircon Hf T_{DM2} ages.

5 . Discussion

5.1 . The Taili adakitic plutons: melting of the Paleoproterozoic mafic lower continental crust

The Taili granitic plutons show uniform composition and share very similar geochemical features with modern adakites and Archean

Table 2
Bulk rock Sr–Nd isotopic compositions of the Taili adakitic pluton.

Sample	t(Ma)	$^{87}Rb/^{86}Sr$	$^{87}Sr/^{86}Sr$	2σ	$I_{Sr}(t)$	$^{147}Sm/^{144}Nd$	$^{143}Nd/^{144}Nd$	2σ	$\varepsilon_{Nd}(0)$	$\varepsilon_{Nd}(t)$	T_{DM1}(Ma)	T_{DM2}(Ma)
13TL02	220	0.335	0.7056879	3	0.704640	0.098	0.5118331	2	−15.7	−12.9	1733	2047
13TL03	220	0.289	0.7065149	3	0.705612	0.091	0.5118161	3	−16.0	−13.1	1654	2059
13TL04	220	0.253	0.7054645	4	0.704674	0.096	0.5118362	5	−15.6	−12.8	1696	2037
13TL05	220	0.343	0.706396	2	0.705323	0.096	0.5118265	4	−15.8	−13.0	1712	2053
13TL06	220	0.240	0.7055803	4	0.704829	0.098	0.5118126	2	−16.1	−13.3	1751	2078

Parameters used in the calculation are as follows: ^{87}Rb decay $\lambda = 1.42 \times 10^{-11}$ year^{-1}; ^{147}Sm decay $\lambda = 6.54 \times 10^{-12}$ year^{-1}; $(^{147}Sm/^{144}Nd)_{CHUR} = 0.1967$, $(^{143}Nd/^{144}Nd)_{CHUR} = 0.512638$; $(^{147}Sm/^{144}Nd)_{DM} = 0.2137$, $(^{143}Nd/^{144}Nd)_{DM} = 0.51315$ (Jacobsen and Wasserburg, 1980).

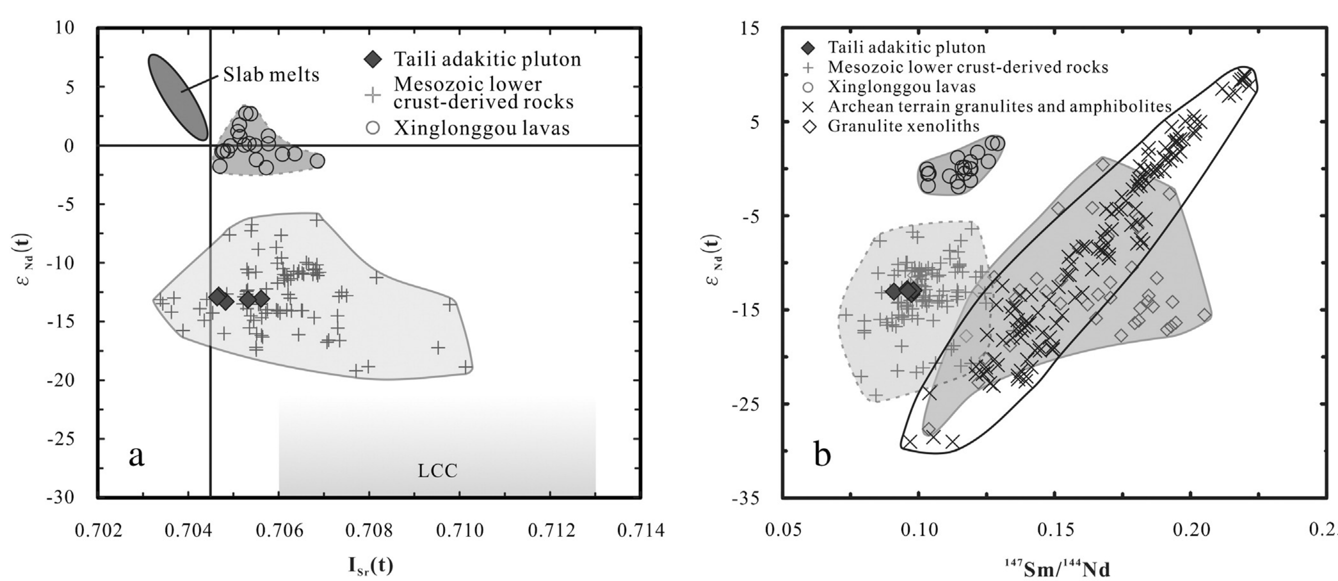

Fig. 7. (a) $\varepsilon_{Nd}(t)$–$I_{Sr}(t)$ diagram and (b) $\varepsilon_{Nd}(t)$–$^{147}Sm/^{144}Nd$ diagram for the Taili adakitic plutons. Also plotted for comparison are those of Xinglonggou lavas, Mesozoic felsic rocks derived from ancient lower crust, granulite xenoliths and terrain granulite and amphibolite in the northern part of the NCC. Data sources: Xinglonggou lavas, Gao et al. (2004); Mesozoic ancient lower crust-derived rocks, Jiang et al. (2007), Ma et al. (2012), Yang et al. (2007) and references therein; granulite xenoliths, Liu et al. (2004), Shao et al. (2000) and references therein; Archean terrain granulites and amphibolites, Jiang et al. (2007), Wu et al. (2005c) and references therein.

TTGs, e.g., high Sr (698.4–1069.4 ppm), La (26.66–36.22 ppm), low Y (5.20–6.64 ppm), Yb (0.33–0.51 ppm) and thus high Sr/Y (119–186) and $(La/Yb)_N$ (41–66) ratios (Fig. 8a,b; Defant and Drummond, 1990; Martin et al., 2005). Their high K_2O and K_2O/Na_2O ratios (mostly > 0.5) are similar to those K-rich "adakites" or "adakitic rocks", such as the Cordillera Blanca granodiorites (Atherton and Petford, 1993), the Cenozoic granitic rocks in Tibet (Chung et al., 2003) and the Jurassic–Cretaceous igneous rocks in eastern China (Rapp et al., 2002; Xiao and Clemens, 2007).

The high SiO_2 and low MgO features of the Taili adakitic plutons agree well with the geochemical features of the high-silica adakites proposed by Martin et al. (2005) (Fig. 8c). They are also characterized by relatively low abundances of compatible elements, such as Cr (31–44 ppm) and Ni (20–25 ppm) (Fig. 9d). Their enriched Sr–Nd isotopic compositions differ significantly from those of the mantle lithosphere beneath the NCC as shown by mantle peridotite xenoliths in Cenozoic volcanic rocks with highly depleted Sr–Nd isotopic compositions ($\varepsilon_{Nd} = 5.5$–12.5; Rudnick et al., 2004). These geochemical characteristics suggest that the parental melts for the Taili adakitic plutons are neither derived from nor interacted with mantle peridotite. The enriched Sr–Nd–Hf isotopic compositions (Figs. 6 and 7) rule out the possibility of young slab melting or melting of newly underplated and thickened mafic lower crust, but point to melting of an ancient lower continental crust.

It was generally thought that the lower continental crust is made of granulite-facies metamorphic rocks (Rudnick and Fountain, 1995). The basement of the NCC consists of Archean terrain granulites and TTGs. Mafic granulite xenoliths in the Mesozoic volcanic rocks are considered to represent the ancient NCC lower crust (Shao et al., 2000; Zheng et al., 2004). These xenoliths reported in the literature are, however, mostly two-pyroxene granulite without garnet, suggesting that they were not formed in the P–T regimes of lower crust. The Mesozoic felsic rocks in the NCC also have highly variable Sr–Nd isotopic compositions (Fig. 7a), suggesting that they must have derived from ancient lower crustal of varying compositions or undergone significant crust–mantle interaction. Comparing to Archean terrain granulites and amphibolites in the NCC, the Taili adakitic plutons show distinguishable Sr–Nd isotopic compositions (Fig. 7b). The Hf T_{DM2} ages (2192–2366 Ma) and Nd

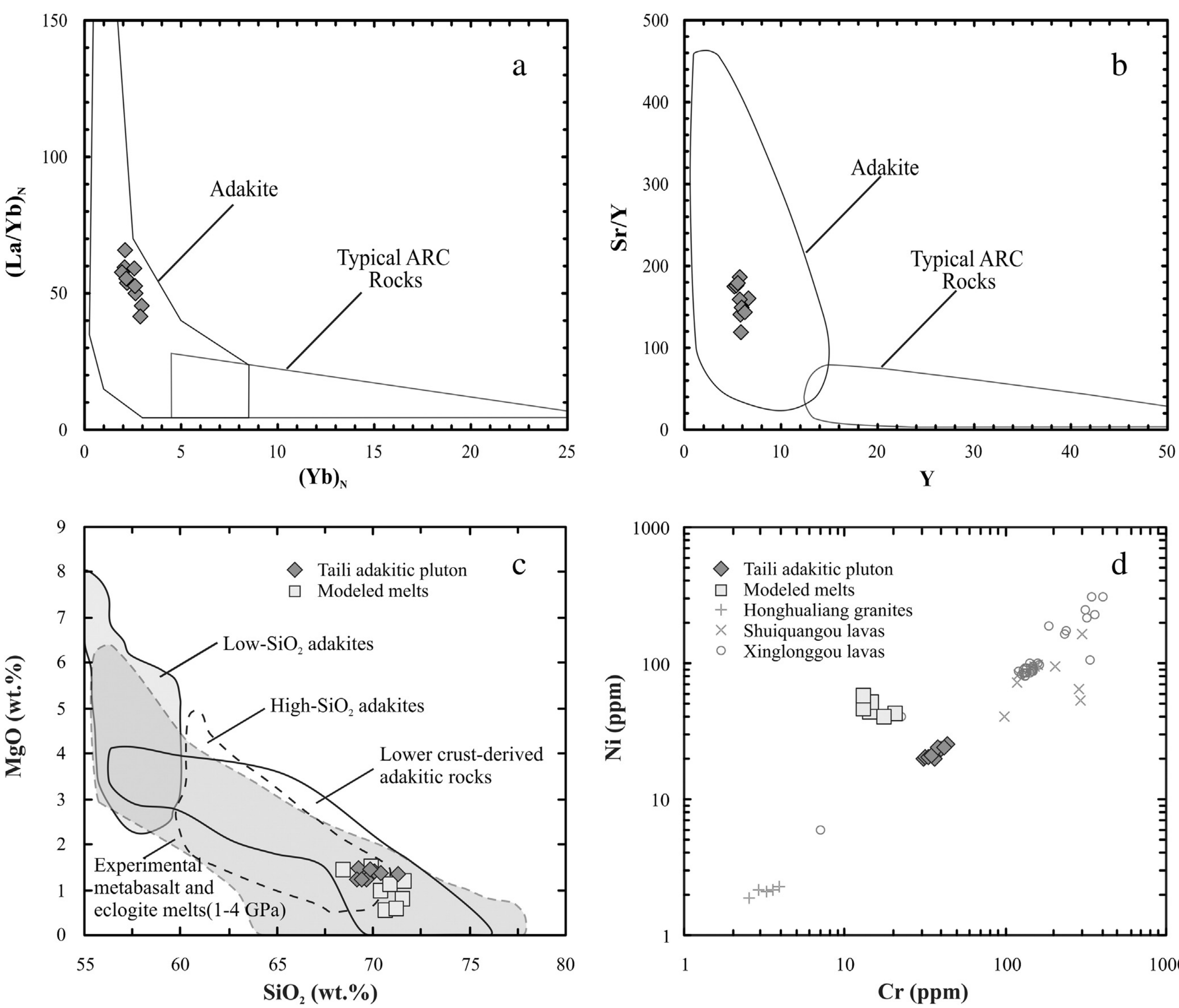

Fig. 8. (a) Chondrite-normalized $(La/Yb)_N$–$(Yb)_N$ diagram and (b) Sr/Y–Y diagram (Defant and Drummond, 1990) for the Taili adakitic plutons; (c) MgO–SiO_2 diagram showing comparison between the Taili adakitic plutons and adakites in various settings, experimental melts and modeled melts. Thickened lower crust-derived rocks (Atherton and Petford, 1993). Experimental meta-basalt and eclogite melts (Qian and Hermann, 2013; Rapp et al., 1991, 2002; Sen and Dunn, 1994; Springer and Seck, 1997 and references therein). (d) Ni–Cr diagram showing the Taili adakitic pluton in comparison with other Mesozoic adakitic rocks in the NCC and the model melts. Note that the modeled Cr and Ni are slightly deviated from the analytical data of the Taili adakitic plutons (Honghualiang adakitic pluton by Jiang et al., 2007; Shuiquangou lavas by Ma et al., 2012; Xinglonggou adakitic lavas by Gao et al., 2004).

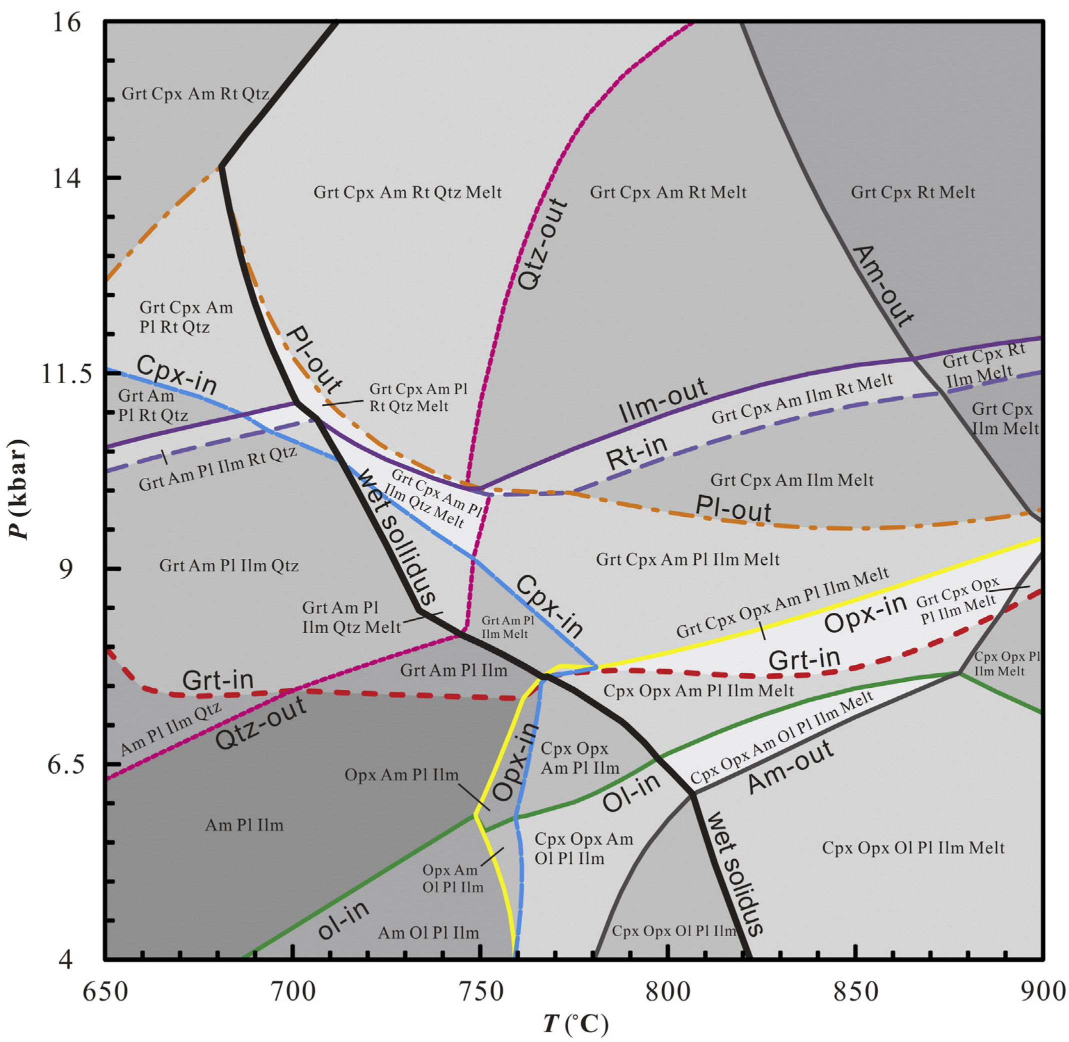

Fig. 9. Equilibrium assemblage diagrams calculated for the water-saturated average composition of the Paleoproterozoic Hengling mafic dykes (Peng et al., 2012). Normalized molar bulk input compositions are SiO_2(47.38)TiO_2(0.59)Al_2O_3(8.54)FeO(10.18)MgO(10.91)CaO(9.38)Na_2O(2.25).

T_{DM2} ages (2078–2037 Ma) seem to point that the Taili adakitic pluton was sourced from mafic magmatic rocks that may have underplated in the Paleoproterozoic (2.3–2.0 Ga), rather than an Archean lower crust.

Considering that mantle plume-related magmatic activities in the Paleoproterozoic (2.3–2.0 Ga) are widespread in Archean cratons worldwide; large volumes of mafic magmas emplaced as dyke swarms present in Antarctica, Australia, Finland, Greenland, North America and South India, which are interpreted to link with intracontinental rifting, mantle plume activities and continental breakups (Ernst and Bleeker, 2010; French and Heaman, 2010; Nilsson et al., 2010). In the NCC, contemporaneous volcanic and plutonic rocks with bimodal magmatic characteristics imply an intracontinental extension and rifting event in the Paleoproterozoic (Peng et al., 2012). Therefore, these mantle plume-related Paleoproterozoic mafic magmas might have underplated the base of the NCC Archean crust, as source rocks of the Taili adakitic plutons in the Late Triassic.

5.2. Modeling for the generation of the Taili adakitic plutons

In order to model the petrogenesis of the Taili adakitic plutons with parental magmas derived from partial melting of the underplated Proterozoic lower crust and to place constraints on *P*–*T* conditions for the formation of the Taili adakitic plutons, we conducted calculations of equilibrium mineral assemblages in a partially molten mafic rock followed by modeling of trace element partition between melts and residual phases at different pressures and melt fractions using the method of Nagel et al. (2012). Based on the two-stage depleted mantle Hf and Nd isotope model ages of the Taili adakitic plutons, the average composition of the Paleoproterozoic Hengling mafic dykes in the NCC (2147 ± 5 Ma; Table 3; Peng et al., 2012) was selected as an approximate source for representing the underplated Paleoproterozoic lower crust. The Paleoproterozoic Hengling mafic dykes are all tholeiitic in composition and their average composition is similar to that of the lower continental crust in terms of trace elements (Table 3; Fig. 11; Rudnick and Gao, 2003). Equilibrium assemblage diagrams under water-saturated condition (Fig. 9) and mineral assemblages during isobaric water-absent partial melting at different pressures (Fig. 10) were calculated using the software package Theriak/Domino (vers. 03.01.12; De Capitani and Petrakakis, 2010) and the database of Holland and Powell (1998) with normalized molar bulk input composition: SiO_2(47.38)TiO_2(0.59) Al_2O_3(8.54)FeO(10.18)MgO(10.91)CaO(9.38)Na_2O(2.25). Fig. 9 can roughly constrain phase relations during partial melting of the mafic source rock, while Fig. 10 gives more reasonable information about the actual fractions of coexisting phases for the subsequent calculation of trace element partitioning. It has been shown that the software package and the database are suitable for predicting the formation of TTG/adakitic melts from mafic rocks (Nagel et al., 2012). Trace element partitioning between melts and residual phases for calculated

Table 3
Trace element composition of the source rock (the average composition of the Paleoproterozoic Hengling mafic dykes) and partition coefficients used in trace element modeling.

		Partition coefficients						
	(ppm)	Rt	Ilm	Pl	Am	Cpx	Opx	Grt
Th	0.750	0.2	0.09	0.095	0.055	0.104	0.13	0.0075
Nb	3.372	96	3	0.239	0.39	0.007	0.01	0.04
Ta	0.332	210	2.7	0.053	0.38	0.028	0.126	0.08
La	9.098	0.006	0.015	0.358	0.319	0.028	0.0003	0.028
Ce	20.40	0.007	0.012	0.339	0.56	0.059	0.0007	0.08
Pr	2.761	0.007	0.011	0.316	0.898	0.116	0.0014	0.15
Sr	296.6	0.036	0.002	6.65	0.389	0.032	0.047	0.019
Nd	11.94	0.008	0.01	0.289	1.32	0.115	0.0028	0.222
Zr	66.94	4.1	2.3	0.078	0.42	0.125	0.031	0.537
Hf	1.923	6	2.4	0.069	0.66	0.208	0.246	0.431
Sm	2.879	0.095	0.009	0.237	2.09	0.259	0.0085	1.43
Eu	0.95	0	0.01	2.17	1.79	0.341	0.68	1.54
Ti	4827	45	12.5	0.08	4.03	0.47	0.5	2.63
Gd	3.025	0.0106	0.011	0.192	2.53	0.422	0.02	4.84
Tb	0.522	0.0111	0.018	0.17	2.6	0.502	0.03	7.80
Dy	3.322	0.0116	0.02	0.15	2.55	0.57	0.043	11.5
Y	18.02	0.0118	0.037	0.138	2.47	0.603	0.054	14.1
Ho	0.702	0.0119	0.035	0.132	2.41	0.616	0.06	15.3
Er	1.965	0.0122	0.067	0.117	2.22	0.640	0.079	18.8
Tm	0.296	0.0124	0.102	0.104	2	0.644	0.101	21.5
Yb	1.918	0.0126	0.13	0.094	1.79	0.635	0.125	23.2
Lu	0.297	0.0127	0.19	0.085	1.59	0.617	0.149	24.1
Cr	125.6	0	2.9	0.15	4.7	0.582	7.97	22
Ni	131.9	0	6.8	1.73	6.12	5.96	7.35	1.2

Data sources: average composition of the Hengling mafic dykes, Peng et al. (2012); partition coefficients, Klein et al. (1997), Klemme et al. (2005), Bédard (2006). Rt, rutile; Ilm, ilmenite; Pl, plagioclase; Am, amphibole; Cpx, clinopyroxent; Opx, orthopyroxene; Grt, garnet.

equilibrium assemblages during isobaric water-absent partial melting was modeled using experimentally determined partition coefficients (Table 3; Klein et al., 1997; Klemme et al., 2005; Bédard, 2006).

Fig. 9 shows the equilibrium assemblage calculated for the average composition of the Hengling mafic dykes under water-saturated condition in the SiTiAlFeMgCaNaHO space. To make the procedures concise and explicit, potassium was not included in the calculation. At lower pressures and temperatures, it forms amphibolite with mineral assemblages of Am + Pl + Ilm or Am + Pl + Ilm + Qtz. Toward higher pressures, garnet appears at >8 kbar, plagioclase disappears at >9.5 kbar, and rutile begin to replace ilmenite at >10 kbar. Clinopyroxene and orthopyroxene begin to form with increasing pressures and/or temperatures. Melting begins when P–T approach the solidus. Because the model assumed water-saturated situations, it strongly overestimates the melt content than in natural systems and the fractions of melts and residual phases should not be employed for modeling the trace element partition between melts and residual phases. Thus, we also calculated equilibrium assemblages and isobaric partial melting under anhydrous conditions at different pressures (10, 12, 14 and 16 kbar).

Fig. 10 shows the variation of mineral assemblages during isobaric anhydrous partial melting of the average composition of the Hengling mafic dykes at different pressures. In all runs, at least 10 wt.% garnet is present at different pressures, and ilmenite is present at lower pressures and rutile at high pressures. Plagioclase is stable in all runs and the amount of plagioclase decreases with increasing pressures. Melt generation is associated with the decomposition of amphibole, which releases water into the system and starts at around 750 °C, leaving a residue of garnet granulite. The amount of melt increases with temperature and decreases with pressure. The calculated major element compositions of melts at fractions of 5 and 10 wt.% are similar to the compositions of the Taili adakitic plutons, except for being rich in Fe and Na and poor in Ca (Table 4). The Taili adakitic plutons are characterized by their relatively high K content and reflect a K-rich source (Moyen and Stevens, 2006; Rapp et al., 2002; Xiao and Clemens, 2007) or low-degree melting process considering that K is highly incompatible during partial melting (Qian and Hermann, 2013).

The modeling of trace element partitioning between melts and residual phases is illustrated in Fig. 11. It shows that melts of 5–10% degree partial melting at 10–12 kbar (780–820 °C) could give a better fit for the Taili adakitic plutons than melts at 14 kbar and 16 kbar. At lower pressures, rutile is not present in residual phases and ilmenite controls the Nb–Ta budget. Toward higher pressures, rutile replaces ilmenite and begins to control the Nb–Ta budget, causing great depletion of Nb and Ta (Klein et al., 1997; Rapp et al., 2003). The Taili adakitic plutons have weaker depletion of Nb and Ta than typical adakites elsewhere (Fig. 4b), implying that the Taili adakitic plutons may be formed at a relatively low pressure. In the 12 kbar run, ilmenite becomes stable at higher temperatures, serving an upper pressure limit of 12 kbar for ilmenite. Thus the pressure for generating the Taili adakitic plutons may not exceed 12 kbar before rutile appears as a stable phase at P ≥ 12 kbars (Figs. 9 and 10). The Sr contents of melts in all runs were not very successfully modeled and lower than those of the Taili adakitic plutons, mainly because the amount of plagioclase was overestimated and the residual plagioclase retained too much Sr. It is evident that Al and Na contents control the stability of plagioclase during partial melting of mafic rocks (Nagel et al., 2012) and the modeled melts are richer in Na than the Taili adakitic plutons (Table 4). Thus the actual source of the Taili adakitic plutons is predicted to be relatively poorer in Al and Na than the average composition of the Hengling mafic dykes in order to account for the high Sr feature of the Taili adakitic plutons. Also it should be noted that the modeled melts have higher Zr and Hf contents than the Taili adakitic plutons due to the fact that zircon was not taken into consideration for clarity and simplicity in the modeling.

Melting experiments of mafic materials suggested that production of adakitic/TTG melts needs a minimum pressure of 15 kbar (ca. 55 km) to stabilize garnet in the residue and account for the high La/Yb and Sr/Y signature (Rapp et al., 1991; Sen and Dunn, 1994; Xiao and Clemens, 2007). However, considering the diverse compositions of adakites/TTGs, a large range of pressures (10–25 kbar) was put forward for the generation of adakites/TTGs (Moyen, 2009; Moyen and Stevens, 2006). Springer and Seck (1997) suggested that partial melts similar to adakites/TTGs in REE can be produced from the lower crust at 10–12.5 kbar and 850–1000 °C. Through experiment, Qian and Hermann (2013) showed that adakitic melts can be produced by partial melting of the lower crust at 10–12.5 kbar and 800–900 °C. Based on thermodynamic calculations and geochemical modeling, Nagel et al. (2012) proposed a similar pressure range of 10–14 kbar for producing TTG melts from arc tholeiites. Our estimation of the *P–T* conditions (10–12 kbar and 780–820 °C) for the generation of the Taili adakitic plutons is probably reasonable, which enable us to conclude that the Taili adakitic plutons was generated from the ancient lower crust beneath the NCC at a depth of ca. 36–43 km.

5.3. Melting of the ancient lower crust by upwelling of the asthenospheric mantle

Melting of the mafic lower continental crust requires excess heat, generally supplied by contemporaneous emplacement of mafic magmas (e.g., Atherton and Petford, 1993; Chung et al., 2003; Wang et al., 2005). During the Triassic, mantle melts may have started to underplate the base of the NCC lower crust, as evidenced by the existence of alkaline intrusives and mafic–ultramafic complexes in the northern part of the NCC (Zhang et al., 2009b, 2012b). Nd–Hf isotopic compositions of Middle–Late Triassic mantle-derived rocks in both the northern and southeast parts of the NCC suggest significant contributions of a young and juvenile mantle component (Ma et al., 2012; Yang et al., 2007; Zhang et al., 2014). The heat provided by the mantle-derived mafic magmas not only caused the granulite-facies metamorphism recorded by lower-crustal granulite xenoliths (Shao et al., 2000), but also induced partial melting the ancient lower crust (Jiang et al., 2007; Ma et al.,

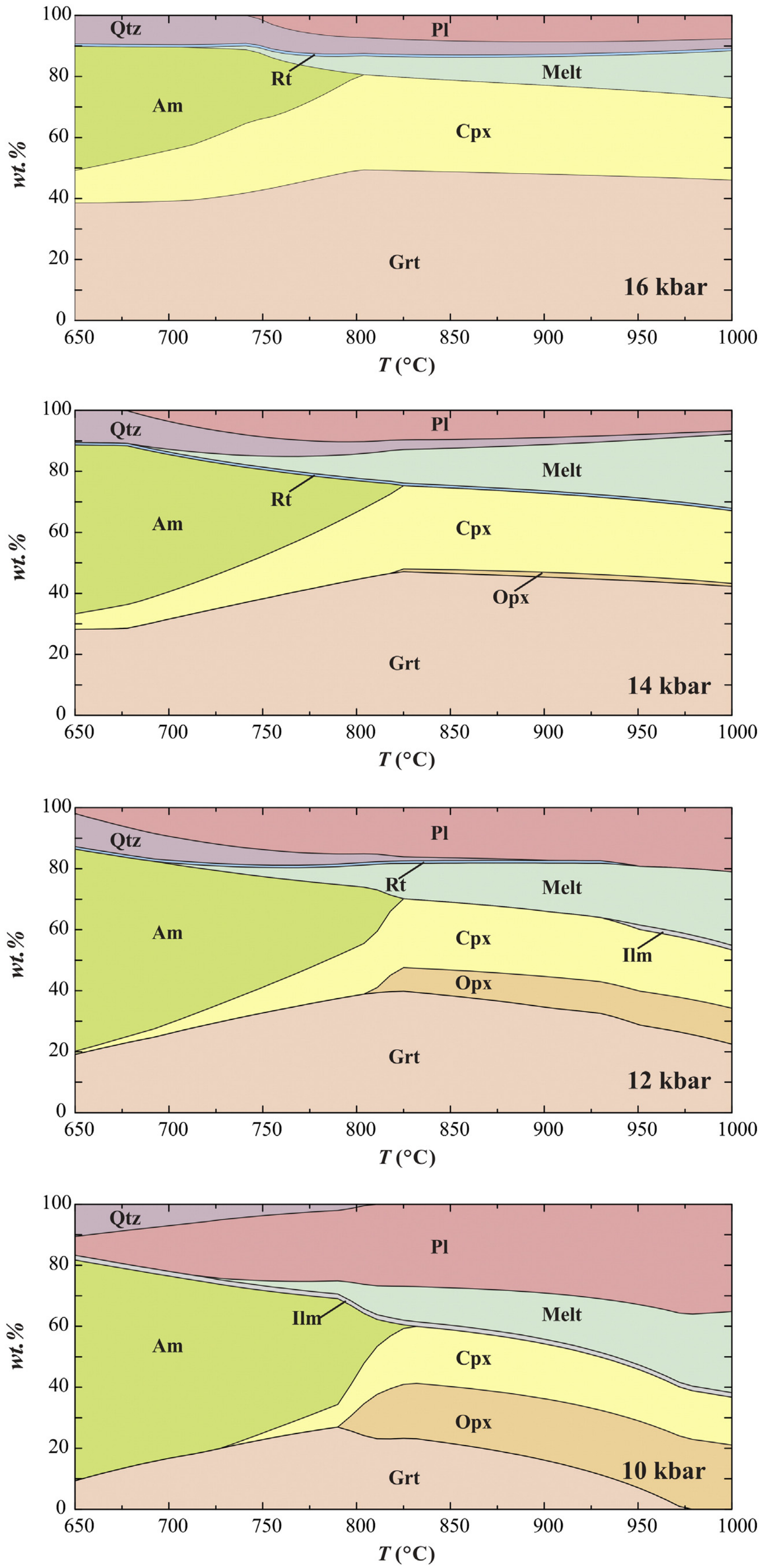

Fig. 10. Calculated stable assemblages during isobaric water-absent partial melting of sample 07DX04 (Peng et al., 2012) of the Paleoproterozoic mafic dykes at 10, 12 and 14 kbar. Amounts of minerals are displayed as weight percent. The calculation assumes pure batch melting.

Table 4
Calculated fractions of coexisting phases and major and trace element compositions of melts at different pressures (10, 12, 14 and 16 kbar) and melt fractions (5% and 10%) during water-absent partial melting.

P (kbar)	10	10	12	12	14	14	16	16
T (°C)	793	818	780	818	773	822	790	916
Calculated fractions of coexisting phases (wt.%)								
Melt	5.00	10.25	5.05	10.30	5.16	10.34	4.88	10.06
Grt	26.35	22.98	36.22	39.70	41.10	46.92	47.96	47.74
Cpx	8.80	17.29	12.51	21.00	17.22	26.91	28.53	28.84
Opx	2.39	16.60	–	5.34	–	0.39	–	–
Pl	23.73	26.97	14.98	15.69	10.03	9.82	6.88	8.62
Ilm	1.54	1.54	–	–	–	–	–	–
Rt	–	–	0.83	0.83	0.83	0.83	0.84	0.84
Am	30.46	4.36	26.68	5.33	20.48	1.45	5.18	–
Qtz	1.73	–	3.72	1.81	5.17	3.33	5.73	3.91
Major element compositions of melts (wt.%)								
SiO_2	71.64	69.92	71.53	70.89	71.21	70.42	70.68	68.44
Al_2O_3	14.37	14.85	15.69	15.51	16.53	16.19	17.04	16.04
FeO	4.32	5.03	2.62	3.30	1.75	2.72	1.48	4.51
MgO	1.17	1.51	0.78	1.10	0.57	0.98	0.55	1.43
CaO	0.91	1.23	0.69	0.87	0.57	0.63	0.52	0.78
Na_2O	7.60	7.45	8.69	8.34	9.36	9.06	9.73	8.80
Trace element concentrations of melts (ppm)								
Th	177.6	170.1	268.2	276.5	383.8	417.5	569.2	468.9
Nb	7.34	4.52	7.94	5.04	8.08	5.26	8.24	5.37
Ta	12.42	14.80	3.53	3.80	3.65	3.90	3.89	3.92
La	1.40	1.60	0.18	0.19	0.18	0.19	0.19	0.19
Ce	39.11	42.90	46.60	49.47	55.76	57.70	83.93	61.61
Pr	65.05	87.76	74.14	93.95	87.36	108.21	134.94	115.53
Sr	6.44	10.48	7.11	10.39	8.28	11.79	12.92	12.57
Nd	21.23	41.41	23.14	38.81	27.08	44.67	44.99	48.10
Zr	181.7	219.9	167.4	175.7	166.2	166.3	173.4	167.2
Hf	4.55	5.72	4.29	4.89	4.41	4.87	4.97	4.93
Sm	2.65	4.98	2.53	3.62	2.66	3.53	3.23	3.59
Eu	0.64	0.81	0.69	0.83	0.75	0.90	0.88	0.93
Ti	1.46	2.30	1.24	1.47	1.20	1.32	1.21	1.31
Gd	0.18	0.27	0.15	0.17	0.14	0.15	0.13	0.15
Tb	0.89	1.23	0.70	0.75	0.65	0.65	0.59	0.64
Dy	4.12	5.56	3.21	3.35	2.94	2.89	2.66	2.85
Y	0.15	0.20	0.12	0.12	0.11	0.10	0.10	0.10
Ho	0.36	0.47	0.27	0.28	0.25	0.24	0.22	0.24
Er	0.05	0.06	0.04	0.04	0.03	0.03	0.03	0.03
Tm	0.30	0.38	0.22	0.22	0.20	0.19	0.18	0.19
Yb	0.04	0.06	0.03	0.03	0.03	0.03	0.03	0.03
Lu	2270	4228	2013	2853	2099	2805	2490	2845
Cr	17.39	20.33	14.12	14.48	13.02	13.08	11.98	12.94
Ni	40.26	42.25	44.45	51.91	46.35	57.25	50.18	57.46
$(La/Yb)_N$	94	82	149	159	199	217	342	236
Sr/Y	43	31	84	83	131	144	214	164

2012). The input of mantle materials could affect the compositions of the melts generated by partial melting of the ancient lower crust, as recorded in the Shuiquangou lavas, which have elevated Cr and Ni contents and higher $\varepsilon_{Nd}(t)$ (−9.9 to −3.9) and $\varepsilon_{Hf}(t)$ (−8.6 to −1.1) values in some samples (Ma et al., 2012). However, the relatively low Cr and Ni contents and low $\varepsilon_{Nd}(t)$ and $\varepsilon_{Hf}(t)$ values of the Taili adakitic plutons (Figs. 6, 7 and 8d), imply negligible input of mantle materials. This is further supported by the modeling of trace element partitioning (Fig. 8d).

5.4. Implications for crustal reworking and onset of the lithosphere thinning beneath the NCC

The NCC had been a stable shield characterized by tectonic inactivity, a thick and refractory lithospheric mantle and low heat flow (Foley, 2008) after the final amalgamation in the Paleoproterozoic (Zhao et al., 2005). Since the Late Paleozoic, the NCC began to lose its stability and experienced a series of intense tectonothermal events, namely, the lithosphere thinning (Menzies et al., 1993; Yang and Wu, 2009; Yang et al., 2008). These events were accompanied by large-scale magmatism (Wu et al., 2005a), deformation (Davis et al., 2001) and mineralization (Yang et al., 2003; Zhu et al., 2012). As a result, the ancient, cratonic lithospheric mantle beneath the NCC was removed and replaced by juvenile lithospheric mantle during the Mesozoic (Menzies et al., 1993; Xu, 2001).

However, it is still not clear if the crust on top of the lithospheric mantle has also been destructed or thinned, and if so, when and how this thinning occurred. Most researchers held the view that the NCC thinning was limited within the mantle lithosphere (Menzies et al., 1993; Niu, 2005), but some researchers believed that part of the crust was also involved in the destruction of the NCC (Gao et al., 2004; Wu et al., 2005a). The average thickness of the intact cratonic crust on Earth is ~40 km (Tedla et al., 2011). The present thickness of the crust of the eastern NCC, however, is only about 30 km (Chen, 2010), which infers that ~10 km of the ancient cratonic crust could have been eroded since the Mesozoic era if the prior crust was in excess of 40 km thick. The Taili adakitic plutons, along with other Mesozoic adakitic rocks in the NCC (e.g., Jiang et al., 2007; Ma et al., 2012), suggest that the ancient lower crust may be involved in the process of the NCC lithosphere thinning through magmatism although such lower crust cannot be

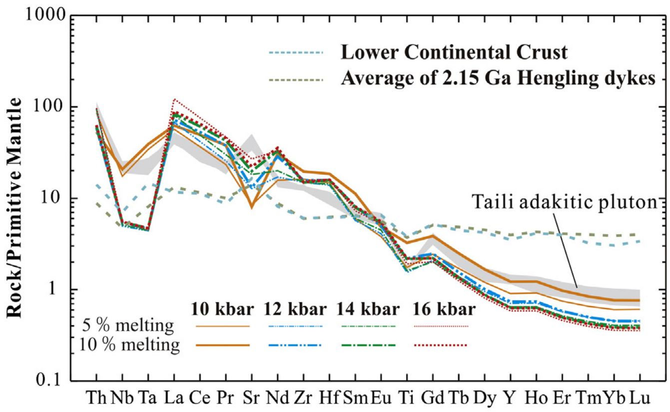

Fig. 11. Primitive mantle-normalized trace element patterns for the Taili adakitic plutons and modeled melts. Colored solid lines indicate compositions of modeled melts at different pressures. Thick lines are calculated for 5% melt, thin lines for 10% melt. Also shown for comparison are the compositions of sample 07DX04 (Peng et al., 2012) of the Paleoproterozoic mafic dykes and lower continental crust (LCC; Rudnick and Gao, 2003). (For interpretation of the references to colour in this figure legend, the reader is referred to the web version of this article.)

delaminated into the asthenospheric mantle because both Mesozoic and Cenozoic basalts contain mantle xenoliths of lithospheric mantle origin.

Adakitic rocks of lower crust origin and contemporaneous mafic magmas are usually associated with extensional settings (Atherton and Petford, 1993; Chung et al., 2003; Jiang et al., 2007). Three possible environments for crustal extension could be: (1) continental rifts; (2) back-arc setting; and (3) diapir of mantle plume. There is no evidence for continental rifting and mantle plume activity in the Mesozoic in the NCC. Considering that the Taili adakitic plutons are located in the central part of the NCC, ~ 300 km to the CAOB in the northwest and ~350 km to Sulu belt in the southeast, we speculate that the contemporaneous, two-sided subduction may be responsible for the extension of the NCC.

Back-arc extension is a common tectonic phenomenon during slab subduction on Earth (e.g., Stern, 2002). This extension can be induced by corner flows in the mantle wedge (e.g., Kelemen et al., 2003), or slab rollback (e.g., Heuret and Lallemand, 2005), and more effectively by trench retreat, which can cause the overriding plate under extension (Niu, 2014). The contemporaneous, two-sided subduction/collision beneath the NCC may create extension from both south and north, which

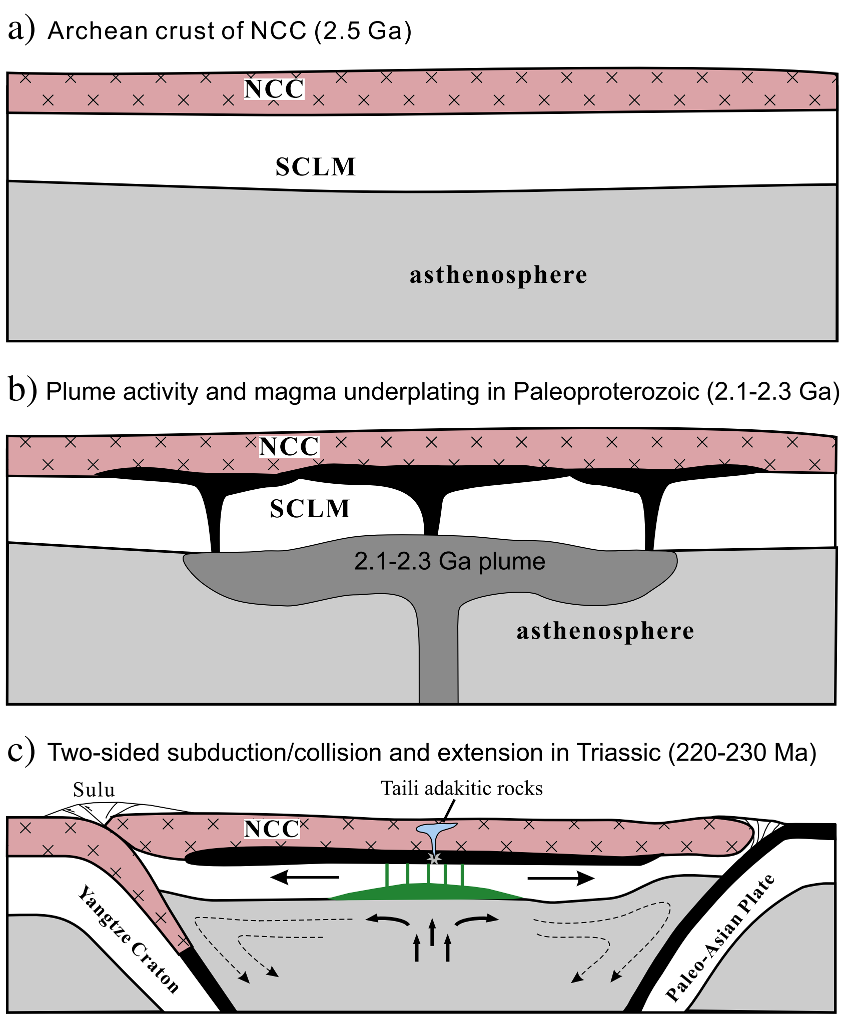

Fig. 12. Cartoons for the forming process of the Taili adakitic plutons (not to scale). (a) In the end of the Archaean, the North China Craton formed with a ~ 2.5 Ga crust and a sub-continental lithospheric mantle. (b) In the Paleoproterozoic, plume-related mafic magmas underplated the base of the crust, formed a thick mafic lower crust. (c) In the Late Paleozoic and Triassic, two-sided subduction/collision toward the NCC, induced corner flow and rollback of the plate, and then caused two-way stretching within the center of the NCC and upwelling and melting of the asthenosphere. The ascending mantle-derived magmas provided heat for melting of the Paleoproterozoic underplated lower crust at depths of 36–43 km, generating the Taili adakitic plutons.

may be suggested by Early –Middle Triassic to the Late Triassic deformation patterns in the northern part of the NCC (Zhang et al., 2014). Under such extensional stress field, there could be lithosphere thinning and passive asthenosphere upwelling within the center of the NCC. The upwelling asthenosphere then experienced decompression melting, formed a large number of Late Triassic igneous rocks in both north and south sides of the NCC. The ascending mantle-derived mafic magmas underplated the base of the crust, providing heat for melting the Paleoproterozoic mafic lower crust. Fig. 12 illustrates the forming process of the Taili adakitic plutons. This scenario cannot be applied to the whole process of the long-lived lithospheric thinning history of the NCC, but offers some alternative/additional perspectives for onset of the lower crust destruction.

6 . Conclusions

(1) The Late Triassic (230–220 Ma) Taili adakitic plutons are characterized by high Sr/Y and $(La/Yb)_N$ ratios, low Cr, Ni and MgO. Their enriched Sr–Nd–Hf isotopic compositions, as well as old Nd or Hf isotope ages, point to a possible source of the Paleoproterozoic mafic lower crust.
(2) Modeling of equilibrium assemblages and trace element partitioning suggests that the Taili adakitic plutons or their parental melts represent 5–10% partial melts of Paleoproterozoic mafic lower crust at 10–12 kbar and 780–820 °C, corresponding to a depth of 36–43 km. However, we suggest that further effort is warranted to verify these melting conditions.
(3) The melting of Paleoproterozoic mafic lower crust accomplished by heating of the possible underplating of mantle-derived melts produced by decompression melting of the upwelling asthenosphere. The upwelling of the asthenosphere was facilitated by mantle wedge corner flow and trench retreat of contemporaneous, two-sided subduction around the NCC. Because trench retreat stops upon continental collision, this place constrains that the related continental collisions may be slightly later than previously thought.
(4) The destruction or lithospheric thinning of the NCC might have begun as early as in the Late Triassic from its margins by subduction and collision of adjacent blocks.

Supplementary data to this article can be found online at http://dx.doi.org/10.1016/j.lithos.2014.11.027.

Acknowledgments

We thank K.J. Hou and C.L. Guo for in-situ LA-MC-ICP-MS zircon Hf isotope analyses, and Z.B. Xiao and W.P. Zhu for Sr–Nd isotope analyses. We thank T.J. Nagel for discussion and help with thermodynamic calculation and trace element modeling. We also thank the two reviewers and Editor-in-chief Andew Kerr for their constructive review comments. This study was supported by the National Key Basic Research Program of China (2013CB429806) and the National Natural Science Foundation of China (Grant Nos. 41372060, 40825007, 41121062, 41130314, 91014003).

References

Andersen, T., 2002. Correction of common lead in U–Pb analyses that do not report ^{204}Pb. Chemical Geology 192, 59–79.
Atherton, M.P., Petford, N., 1993. Generation of sodium-rich magmas from newly underplated basaltic crust. Nature 362, 144–146.
Bédard, J.H., 2006. A catalytic delamination-driven model for coupled genesis of Archaean crust and sub-continental lithospheric mantle. Geochimica et Cosmochimica Acta 70, 1188–1214.
Black, L.P., Kamo, S.L., Allen, C.M., Aleinikoff, J.N., Davis, D.W., Korsch, R.J., Foudoulis, C., 2003. TEMORA 1: a new zircon standard for Phanerozoic U–Pb geochronology. Chemical Geology 200, 155–170.
Castillo, P.R., 2012. Adakite petrogenesis. Lithos 134–135, 304–316.
Chen, L., 2010. Concordant structural variations from the surface to the base of the upper mantle in the North China Craton and its tectonic implications. Lithos 120, 96–115.
Chung, S.L., Liu, D.Y., Ji, J.Q., Chu, M.F., Lee, H.Y., Wen, D.J., Lo, C.H., Lee, T.Y., Qian, Q., Zhang, Q., 2003. Adakites from continental collision zones: Melting of thickened lower crust beneath southern Tibet. Geology 31, 1021–1024.
Davis, G.A., Zheng, Y.D., Wang, C.Q., Darby, B.J., Zhang, C.H., Gehrels, G., 2001. Mesozoic tectonic evolution of the Yangshan fold and thrust belt, with emphasis on Hebei and Liaoning provinces, northern China. Geological Society of America Memoirs 194, 171–197.
De Capitani, C., Petrakakis, K., 2010. The computation of equilibrium assemblage diagrams with Theriak/Domino software. American Mineralogist 95, 1006–1016.
Defant, M.J., Drummond, M.S., 1990. Derivation of some modern arc magmas by melting of young subducted lithosphere. Nature 347, 662–665.
Defant, M.J., Clarck, L.F., Stewart, R.H., Drummond, M.S., de Boer, J.Z., Maury, R.C., Bellon, H., Jackson, T.E., Restrepo, J.F., 1991. Andesite and dacite genesisvia contrasting processes: the geology and geochemistry of El volcano. Panama. Contributions to Mineralogy and Petrology 106, 309–324.
Ernst, R., Bleeker, W., 2010. Large igneous provinces (LIPs), giant dyke swarms, and mantle plumes: significance for breakup events within Canada and adjacent regions from 2.5 Ga to the Present. Canadian Journal of Earth Sciences 47, 695–739.
Foley, S.F., 2008. Rejuvenation and erosion of the cratonic lithosphere. Nature Geoscience 1, 503–510.
French, J.E., Heaman, L.M., 2010. Precise U–Pb dating of Paleoproterozoic mafic dyke swarms of the Dharwar craton, India: implications for the existence of the Neoarchean supercraton Sclavia. Precambrian Research 183, 416–441.
Gao, S., Rudnick, R.L., Yuan, H.L., Liu, X.M., Liu, Y.S., Xu, W.L., Ling, W.L., Ayers, J., Wang, X.C., Wang, Q.H., 2004. Recycling lower continental crust in the North China craton. Nature 432, 892–897.
Heuret, A., Lallemand, S., 2005. Plate motions, slab dynamics and back-arc deformation. Physics of the Earth and Planetary Interiors 149, 31–51.
Hofmann, A.W., 1997. Mantle geochemistry: the message from oceanic volcanism. Nature 385, 219–229.
Holland, T.J.B., Powell, R., 1998. An internally consistent thermodynamic data set for phases of petrological interest. Journal of Metamorphic Geology 16, 309–343.
Hou, K.J., Li, Y.H., Zou, T.R., Qu, X.M., Shi, Y.R., Xie, G.Q., 2007. Laser ablation-MC-ICP-MS technique for Hf isotope microanalysis of zircon and its geological applications. Acta Petrologica Sinica 23 (10), 2595–2604 (In Chinese with English abstract).
Jacobsen, S.B., Wasserburg, G.J., 1980. Sm–Nd isotopic evolution of chondrites. Earth and Planetary Science Letters 50, 139–155.
Jiang, N., Liu, Y.S., Zhou, W.G., Yang, J.H., Zhang, S.Q., 2007. Derivation of Mesozoic adakitic magmas from ancient lower crust in the North China craton. Geochimica et Cosmochimica Acta 71, 2591–2608.
Kelemen, P.B., Rilling, J.L., Parmentier, E.M., Mehl, L., Hacker, B.R., 2003. Thermal structure due to solid-state flow in the mantle wedge beneath arcs. In: Eiler, J. (Ed.), Inside the Subduction Factory. American Geophysical Union, Washington, DC, pp. 293–311.
Klein, M., Stosch, H.G., Seck, H.A., 1997. Partitioning of high field-strength and rare-earth elements between amphibole and quartz-dioritic to tonalitic melts: an experimental study. Chemical Geology 138, 257–271.
Klemme, S., Prowatke, S., Hametner, K., Günther, D., 2005. Partitioning of trace elements between rutile and silicate melts: implications for subduction zones. Geochimica et Cosmochimica Acta 69, 2361–2371.
Li, S.G., Xiao, Y.L., Liou, D.L., Chen, Y.Z., Ge, N.J., Zhang, Z.Q., Sun, S.S., Cong, B.L., Zhang, R.Y., Hart, S.R., Wang, S.S., 1993. Collision of the North China and Yangtse Blocks and formation of coesite-bearing eclogites: timing and processes. Chemical Geology 109, 89–111.
Li, S.Z., Zhao, G.C., Dai, L.M., Liu, X., Zhou, L.H., Santosh, M., Suo, Y.H., 2012. Mesozoic basins in eastern China and their bearing on the deconstruction of the North China Craton. Journal of Asian Earth Sciences 47, 64–79.
Liu, D.Y., Nutman, A.P., Compston, W., Wu, J.S., Shen, Q.H., 1992. Remnants of ≥ 3800 Ma crust in the Chinese part of the Sino-Korean craton. Geology 20, 339–342.
Liu, Y.S., Gao, S., Yuan, H.L., Zhou, L., Liu, X.M., Wang, X.C., Hu, Z.C., Wang, L.S., 2004. U–Pb zircon ages and Nd, Sr, and Pb isotopes of lower crustal xenoliths from North China Craton: insights on evolution of lower continental crust. Chemical Geology 211, 87–109.
Liu, J.L., Davis, G.A., Ji, M., Guan, H.M., Bai, X.D., 2008. Crustal detachment and destruction of the Keel of North China Craton: constraints from Late Mesozoic extensional structures. Earth Science Frontiers 15, 72–81.
Ludwig, K.R., 2003. User's Manual for Isoplot 3.0: a Geochronological Toolkit for Microsoft Excel. Berkeley Geochronology Centre, Special Publication.
Ma, Q., Zheng, J.P., Griffin, W.L., Zhang, M., Tang, H.Y., Su, Y.P., Ping, X.Q., 2012. Triassic "adakitic" rocks in an extensional setting (North China): melts from the cratonic lower crust. Lithos 149, 159–173.
Martin, H., Smithies, R.H., Rapp, R., Moyen, J.F., Champion, D., 2005. An overview of adakite, tonalite–trondhjemite–granodiorite (TTG), and sanukitoid: relationships and some implications for crustal evolution. Lithos 79, 1–24.
Menzies, M.A., Fan, W.M., Zhang, M., 1993. Palaeozoic and Cenozoic lithoprobes and the loss of >120 km of Archaean lithosphere, Sino-Korean craton, China. Geological Society, London, Special Publications 76, 71–81.
Morel, M.L.A., Nebel, O., Nebel-Jacobsen, Y.J., Miller, J.S., Vroon, P.Z., 2008. Hafnium isotope characterization of the GJ-1 zircon reference material by solution and laser-ablation MC-ICPMS. Chemical Geology 255, 231–235.
Moyen, J.F., 2009. High Sr/Y and La/Yb ratios: the meaning of the "adakitic signature". Lithos 112, 556–574.
Moyen, J.F., Stevens, G., 2006. Experimental constraints on TTG petrogenesis: implications for Archean geodynamics, Archean Geodynamics and Environments. AGU, Washington, DC.

Nagel, T.J., Hoffmann, J.E., Münker, C., 2012. Generation of Eoarchean tonalite–trondhjemite–granodiorite series from thickened mafic arc crust. Geology 40, 375–378.
Nilsson, M.K.M., Söderlund, U., Ernst, R.E., Hamilton, M.A., Scherstén, A., Armitage, P.E.B., 2010. Precise U–Pb baddeleyite ages of mafic dykes and intrusions in southern West Greenland and implications for a possible reconstruction with the Superior craton. Precambrian Research 183, 399–415.
Niu, Y.L., 2005. Generation and evolution of basaltic magmas: some basic concepts and a new view on the origin of Mesozoic–Cenozoic basaltic volcanism in eastern China. Geological Journal of China Universities 11, 9–46 (in English with English abstract).
Niu, Y.L., 2014. Geological understanding of plate tectonics: basic concepts, illustrations, examples and new perspectives. Global Tectonics and Metallogeny 10. http://dx.doi.org/10.1127/gtm/2014/0009 (24 pp.).
Peng, P., Zhai, M.G., Ernst, R., Guo, J.H., Liu, F., Hu, B., 2008. A 1.78 Ga large igneous province in the North China Craton: the Xiong'er Volcanic Province and the North China dyke swarm. Lithos 101 (3–4), 260–280.
Peng, P., Bleeker, W., Ernst, R.E., Söderlund, U., McNicoll, V., 2011. U–Pb baddeleyite ages, distribution and geochemistry of 925 Ma mafic dykes and 900 Ma sills in the North China craton: evidence for a Neoproterozoic mantle plume. Lithos 127, 210–221.
Peng, P., Guo, J.H., Zhai, M.G., Windley, B.F., Li, T.S., Liu, F., 2012. Genesis of the Hengling magmatic belt in the North China Craton: implications for Paleoproterozoic tectonics. Lithos 148, 27–44.
Qian, Q., Hermann, J., 2013. Partial melting of lower crust at 10–15 kbar: constraints on adakite and TTG formation. Contributions to Mineralogy and Petrology 1–30.
Rapp, R.P., Watson, E.B., Miller, C.F., 1991. Partial melting of amphibolite/eclogite and the origin of Archean trondhjemites and tonalites. Precambrian Research 51, 1–25.
Rapp, R.P., Xiao, L., Nobu, S., 2002. Experimental constraints on the origin of potassium-rich adakties in eastern China. Acta Petrologica Sinica 293–302.
Rapp, R.P., Shimizu, N., Norman, M.D., 2003. Growth of early continental crust by partial melting of eclogite. Nature 425, 605–609.
Rudnick, R.L., Fountain, D.M., 1995. Nature and composition of the continental crust: a lower crustal perspective. Reviews of Geophysics 33, 267–309.
Rudnick, R.L., Gao, S., 2003. Composition of the continental crust. Treatise on Geochemistry 1–64.
Rudnick, R.L., Gao, S., Ling, W.L., Liu, Y.S., McDonough, W.F., 2004. Petrology and geochemistry of spinel peridotite xenoliths from Hannuoba and Qixia, North China craton. Lithos 77, 609–637.
Samaniego, P., Martin, H., Monzier, M., Robin, C., Fornari, M., Eissen, J.-p., Cotten, J., 2005. Temporal evolution of magmatism in the northern volcanic zone of the Andes: The geology and petrology of Cayambe Volcanic Complex (Ecuador). Journal of Petrology 46, 2225–2252.
Sen, C., Dunn, T., 1994. Dehydration melting of a basaltic composition amphibolite at 1.5 and 2.0 GPa: implications for the origin of adakites. Contributions to Mineralogy and Petrology 117, 394–409.
Shao, J.A., Han, Q.J., Li, H.M., 2000. Discovery of the Early Mesozoic granulite xenoliths in North China Craton. Science China Earth Science 43, 245–252.
Song, S.G., Niu, Y.L., Wei, C.J., Ji, J.Q., Su, L., 2010. Metamorphism, anatexis, zircon ages and tectonic evolution of the Gongshan block in the northern Indochina continent—an eastern extension of the Lhasa Block. Lithos 120, 327–346.
Song, S.G., Niu, Y.L., Su, L., Wei, C.J., Zhang, L.F., 2014. Adakitic (tonalitic–trondhjemitic) magmas resulting from eclogite decompression and dehydration melting during exhumation in response to continental collision. Geochimica et Cosmochimica Acta 130, 42–62.
Springer, W., Seck, H.A., 1997. Partial fusion of basic granulites at 5 to 15 kbar: implications for the origin of TTG magmas. Contributions to Mineralogy and Petrology 127, 30–45.
Stern, R.J., 2002. Subduction zones. Review of Geophysics 40 (4), 1012. http://dx.doi.org/10.1029/2001RG000108.
Sun, S.S., McDonough, W.F., 1989. Chemical and isotopic systematics of oceanic basalts: implications for mantle composition and processes. Geological Society, London, Special Publications 42, 313–345.
Tedla, G.E., Meijde, M.v.d., Nyblade, A.A., Meer, F.D.v.d., 2011. A crustal thickness map of Africa derived from a global gravity field model using Euler deconvolution. Geophysical Journal International 187, 1–9.
Wang, Q., McDermott, F., Xu, J.F., Bellon, H., Zhu, Y.T., 2005. Cenozoic K-rich adakitic volcanic rocks in the Hohxil area, northern Tibet: lower-crustal melting in an intracontinental setting. Geology 33, 465–468.
Wiedenbeck, M., AllÉ, P., Corfu, F., Griffin, W.L., Meier, M., Oberli, F., Quadt, A.V., Roddick, J.C., Spiegel, W., 1995. Three natural zircon standards for U–Th–Pb, Lu–Hf, trace element and REE analyses. Geostandards Newsletter 19, 1–23.
Windley, B.F., Alexeiev, D., Xiao, W., Kröner, A., Badarch, G., 2007. Tectonic models for accretion of the Central Asian Orogenic Belt. Journal of the Geological Society 164, 31–47.
Wu, F.Y., Lin, J.Q., Wilde, S.A., Zhang, X.O., Yang, J.H., 2005a. Nature and significance of the Early Cretaceous giant igneous event in eastern China. Earth and Planetary Science Letters 233, 103–119.
Wu, F.Y., Yang, J.H., Wilde, S.A., Zhang, X.O., 2005b. Geochronology, petrogenesis and tectonic implications of Jurassic granites in the Liaodong Peninsula, NE China. Chemical Geology 221, 127–156.
Wu, F.Y., Zhao, G.C., Wilde, S.A., Sun, D.Y., 2005c. Nd isotopic constraints on crustal formation in the North China Craton. Journal of Asian Earth Sciences 24, 523–545.
Wu, F.Y., Yang, Y.H., Xie, L.W., Yang, J.H., Xu, P., 2006. Hf isotopic compositions of the standard zircons and baddeleyites used in U–Pb geochronology. Chemical Geology 234, 105–126.
Xiao, L., Clemens, J.D., 2007. Origin of potassic (C-type) adakite magmas: experimental and field constraints. Lithos 95, 399–414.
Xu, Y.G., 2001. Thermo-tectonic destruction of the Archean lithospheric keel beneath eastern China: evidence, timing and mechanism. Physics and Chemistry of the Earth, Part A: Solid Earth and Geodesy 26, 747–757.
Xu, J.F., Shinjo, R., Defant, M.J., Wang, Q., Rapp, R.P., 2002. Origin of Mesozoic adakitic intrusive rocks in the Ningzhen area of east China: partial melting of delaminated lower continental crust? Geology 30, 1111–1114.
Xu, Y.G., Li, H.Y., Pang, C.J., He, B., 2009. On the timing and duration of the destruction of the North China Craton. Chinese Science Bulletin 54, 3379–3396.
Yan, G.H., Mu, B.L., Xu, B.L., He, G.Q., Tan, L.K., Zhao, H., He, Z.F., Zhang, R.H., Qiao, G.S., 1999. Triassic alkaline intrusives in the Yanliao–Yinshan area: their chronology, Sr, Nd and Pb isotopic characteristics and their implication. Science China Earth Science 42, 582–587.
Yang, J.H., Wu, F.Y., 2009. Triassic magmatism and its relation to decratonization in the eastern North China Craton. Science China Earth Science 52, 1319–1330.
Yang, J.H., Wu, F.Y., Wilde, S.A., 2003. A review of the geodynamic setting of large-scale Late Mesozoic gold mineralization in the North China Craton: an association with lithospheric thinning. Ore Geology Reviews 23, 125–152.
Yang, J.H., Sun, J.F., Chen, F.K., Wilde, S.A., Wu, F.Y., 2007. Sources and Petrogenesis of Late Triassic Dolerite Dikes in the Liaodong Peninsula: implications for post-collisional lithosphere thinning of the Eastern North China Craton. Journal of Petrology 48, 1973–1997.
Yang, J.H., Wu, F.Y., Wilde, S.A., Belousova, E., Griffin, W.L., 2008. Mesozoic decratonization of the North China block. Geology 36, 467–470.
Yang, J.H., O'Reilly, S., Walker, R.J., Griffin, W., Wu, F.Y., Zhang, M., Pearson, N., 2010. Diachronous decratonization of the Sino-Korean craton: geochemistry of mantle xenoliths from North Korea. Geology 38, 799–802.
Zhang, K.J., 2012. Destruction of the North China Craton: lithosphere folding-induced removal of lithospheric mantle? Journal of Geodynamics 53, 8–17.
Zhang, H.F., Sun, M., Zhou, X.H., Fan, W.M., Zhai, M.G., Yin, J.F., 2002. Mesozoic lithosphere destruction beneath the North China Craton: evidence from major-, trace-element and Sr–Nd–Pb isotope studies of Fangcheng basalts. Contributions to Mineralogy and Petrology 144, 241–254.
Zhang, H.F., Nakamura, E., Kobayashi, K., Zhang, J., Ying, J.F., Tang, Y.J., Niu, L.F., 2007. Transformation of subcontinental lithospheric mantle through peridotite–melt reaction: evidence from a highly fertile mantle xenolith from the North China craton. International Geology Review 49, 658–679.
Zhang, S.H., Zhao, Y., Yang, Z.Y., He, Z.F., Wu, H., 2009a. The 1.35 Ga diabase sills from the northern North China Craton: implications for breakup of the Columbia (Nuna) supercontinent. Earth and Planetary Science Letters 288, 588–600.
Zhang, S.H., Zhao, Y., Liu, X.C., Liu, D.Y., Chen, F.K., Xie, L.W., Chen, H.H., 2009b. Late Paleozoic to Early Mesozoic mafic–ultramafic complexes from the northern North China Block: constraints on the composition and evolution of the lithospheric mantle. Lithos 110, 229–246.
Zhang, H.F., Zhou, M.F., Sun, M., Zhou, X.H., 2010. The origin of Mengyin and Fuxian diamondiferous kimberlites from the North China Craton: implication for Palaeozoic subducted oceanic slab–mantle interaction. Journal of Asian Earth Sciences 37, 425–437.
Zhang, S.H., Zhao, Y., Santosh, M., 2012a. Mid-Mesoproterozoic bimodal magmatic rocks in the northern North China Craton: implications for magmatism related to breakup of the Columbia supercontinent. Precambrian Research 222–223, 339–367.
Zhang, S.H., Zhao, Y., Ye, H., Hou, K.-J., Li, C.-F., 2012b. Early Mesozoic alkaline complexes in the northern North China Craton: implications for cratonic lithospheric destruction. Lithos 155, 1–18.
Zhang, S.H., Zhao, Y., Davis, G.A., Ye, H., Wu, F., 2014. Temporal and spatial variations of Mesozoic magmatism and deformation in the North China Craton: implications for lithospheric thinning and decratonization. Earth-Science Reviews 131, 49–87.
Zhao, G.C., Sun, M., Wilde, S.A., Li, S.Z., 2005. Late Archean to Paleoproterozoic evolution of the North China Craton: key issues revisited. Precambrian Research 136, 177–202.
Zheng, J.P., Griffin, W.L., O'Reilly, S., Lu, F.X., Yu, C.M., Zhang, M., Li, H.M., 2004. U–Pb and Hf-isotope analysis of zircons in mafic xenoliths from Fuxian kimberlites: evolution of the lower crust beneath the North China craton. Contributions to Mineralogy and Petrology 148, 79–103.
Zhu, R.X., Xu, Y.G., Zhu, G., Zhang, H.F., Xia, Q.K., Zheng, T.Y., 2012. Destruction of the north China craton. Science in China — Earth Science 55, 1565–1587.